大阪大学
OSAKA UNIVERSITY

Arid5a augments tryptophan metabolism and chemokine expression to promote the immune evasion of mesenchymal tumor subtypes.

Gyanu Parajuli

Supervisor: Prof. Tadamitsu Kishimoto (MD,PhD)

Department of Immune Regulation

September 2021

Table of contents **Page no.**

Abbreviation:

EMT	Epithelial to Mesenchymal Transition
EMT-TFs	EMT-Transcription Factors
TME	Tumor Microenvironment
TILs	Tumor infiltrating leukocytes
ICIs	Immune checkpoint inhibitors
PDAC	Pancreatic ductal adenocarcinoma
CRC	Colorectal cancer
Kyn	Kynurenine
Trp	Tryptophan
AhR	Aryl hydrocarbon receptor
gMDSCs	Granulocytic myeloid-derived suppressor cells
Treg	Regulatory T cells
Ido1	Indoleamine 2,3-dioxygenase 1
CCR	C-C motif chemokine-receptor
CCL	C-C motif ligand
RBP	RNA binding protein
Arid5a	AT-rich interaction domain-containing protein 5a

Figures:

Tables:

Abstract

The acquisition of mesenchymal traits in immunologically cold tumors leads to immune evasion. However, the underlying molecular mechanisms that link tumor immune evasiveness and mesenchymal phenotypes remain unclear. In this study, I found that the expression levels of AT-rich interaction domain-containing protein 5a (Arid5a), an RNA-binding protein, is substantially increased in mesenchymal tumor subtypes. The deletion of Arid5a in tumor cell lines enhanced antitumor immunity in immunocompetent mice but not in immunodeficient mice, highlighting the role of Arid5a in immune evasion. Furthermore, an Arid5a-deficient tumor microenvironment was shown to have robust antitumor immunity, as manifested by the suppressed infiltration of granulocytic myeloid-derived suppressor cells and regulatory T-cells, whereas infiltrated T-lymphocytes were more cytotoxic and less exhausted. Mechanistically, Arid5a stabilized *Ido1* and *Ccl2* mRNAs and augmented their expression, resulting in enhanced tryptophan catabolism and an immunosuppressive tumor microenvironment. Furthermore, Arid5a expression was substantially increased in mesenchymal subtypes of pancreatic ductal adenocarcinoma (PDAC) and colorectal cancers (CRC), and Arid5a promoted TGF-β-induced and IL-6-induced epithelial-mesenchymal transition and acquisition of invasiveness in PDAC. Thus, my findings unraveled a novel role of Arid5a as a genetic driver of the immune evasion of mesenchymal tumors. My data expands the role of Arid5a beyond inflammatory diseases, and suggest Arid5a as a promising target for the treatment of immunotolerant malignant tumors.

Introduction

Our body comprises millions of cells, which originated from a single cell with phenotypic variants resulting from specific expression of a defined transcriptome that regulates further functional diversity(1). During embryogenesis, epithelial cells show high plasticity and ability to switch back and forth between epithelial and mesenchymal phenotype through processes known as epithelial-mesenchymal transition (EMT) and mesenchymal-epithelial transition (MET), respectively to support the organization of embryonic development and differentiation(1–3). Following completion of organ development, epithelial cells typically execute specialized organ specific functions(2, 4, 5). It has been proposed that epithelial cells reach the state of terminal differentiation, and that this state is permanent. This notion has been challenged by many observations showing that terminally differentiated epithelial cells, through EMT, can change their phenotype under the influence of repair-associated or pathological stress(2). Thus, EMT is now established as a common mechanism in embryonic development, wound healing, tissue regeneration, organ fibrosis, and initiating invasive and metastatic behavior in epithelial cancer cells(6). EMT is triggered when cells receive signals, such as TGF-β or hypoxia, from their microenvironment during embryonic development and in certain disease states(7).

EMT is driven by EMT-activating transcription factors (EMT-TFs), mainly of the SNAIL, TWIST and ZEB families(6, 8). EMT-TFs play crucial role in all stages of cancer progression from initiation, primary tumor growth, invasion, and metastasis, tumor stemness, and resistance to therapy(9). The EMT program has been previously considered a binary switch from fully epithelial to fully mesenchymal phenotypes. However, it has recently been proposed that EMT is a sequential process involving intermediate hybrid epithelial and mesenchymal phenotypes (a partial EMT), in which individual cells express both epithelial and mesenchymal markers, has observed in developmental processes and wound healing, and

carcinoma(10). During progression from primary tumor to metastasis, cancer cells need to adapt to permanently changing and often hostile environments. This plasticity of tumor cells is mediated by EMT-TFs, which is reflected by their association with poor clinical outcome in wide range of tumor types(11–13).

Cancers grow within complex highly heterogenous tissue environments called the tumor microenvironment (TME). The TME is considered as the cancer's ecosystem, which comprises diverse innate and adaptive immune cells, together with stromal cells, vascular networks, and many other cellular and noncellular components(14, 15). The TME of mesenchymal tumors is generally immunosuppressive as indicated by the abundance of immunosuppressive cells, such as tumor-associated macrophages (TAMs), myeloid-derived suppressor cells (MDSCs), and regulatory T (Treg) cells on the expense of tumor-fighting effector cells, such as cytotoxic CD8 T cells, CD4 Th1, natural killer (NK) cells(11, 16–19). The density, diversity and functionality of tumor-infiltrating immune cells play important role in cancer diagnosis and designing treatment modalities(20). Thus, understanding the differential composition of immune cells in the TME represents an important factor that is closely related to prognosis and prediction of treatment efficacy(14, 21).

Immunotherapy is a paradigm shift in the treatment of advanced cancers(14, 22, 23). Surgery, radiotherapy, chemotherapy, and targeted pathway inhibition with small molecules showed minimal response for patients with metastatic solid tumors(24, 25). Particularly, immune checkpoint-targeting antibody therapy can induce long-lasting tumor regression, and appears to be more effective than any other type of treatment for patients with tumors that have already metastasized. However, the majority of tumors shows resistance to immune checkpoint blockade(26–28). Although a possible explanation for this is the plasticity and heterogeneity of the tumors themselves and their microenvironment, there are still many

issues to be solved towards understanding the mechanism by which advanced cancers avoid immunosurveillance.

Tumors are generally classified as so-called hot and cold tumors based on the abundance of tumor-infiltrating lymphocytes (TILs)(22, 28). Hot tumors are T-cell inflamed and demonstrate an initial immune response, which is weakened by the upregulation of immune checkpoints or by an increase in the number of suppressive immune cells(28, 29). By contrast, cold tumors lack a sufficient number of pre-existing TILs, and are thus known as nonimmunogenic tumors(20, 22, 24). Exhausted T cells and suppressive immune cells such as gMDSCs, TAMs, Tregs are abundant in the cold TME whereas hot tumor shows high infiltration of anti-tumor immune cells including effector T cells, DC, NK, NKT cells(30). Tumor undergoes immune evasion through the disruption of the anti-tumor immune homeostasis in the TME. Immune evasion is a crucial cancer hallmark, often accomplished by the increased activation of an immune checkpoint signal, such as the programmed death 1 (PD-1)/PD-1 ligand 1 axis, or through the accumulation of immunosuppressive metabolites (18, 24, 31, 32). Hot tumors fully or partially respond to immune checkpoint blockade (ICBs). Cold tumors, on the other hand, are refractory to most immunotherapies(20, 29, 33, 34). Most of the cold tumors including prostate cancer, glioblastoma colorectal carcinoma (CRC), and pancreatic ductal adenocarcinoma (PDAC) are resistant to ICBs(14, 24, 30). In particular, a subtype of these cancers that shows the tumor-intrinsic mesenchymal phenotype has been reported to facilitate immune evasion via crosstalk with stromal immune cells in the TME(12, 35). Thus, there are numerous studies focusing on converting cold tumor to hot tumors, while success rate is very limited.

Cancer cells evolve various strategies to evade immune surveillance. A key strategy is to develop and maintain a highly immunosuppressive and metabolically stressed TME, which form a major barrier hindering effective antitumor immunity(36). For example, many tumor

cells engage aerobic glycolysis even in the presence of oxygen to support biosynthetic pathways important for their growth(37). Similarly, activated T cells depend mostly on glycolysis to support cellular proliferation and effector functions(37, 38). Thus, tumor cells limit the function of antitumor T cells through competing for limited nutrients. Moreover, certain metabolites secreted within the TME by tumor cells, TILs, and other immune or stromal cells may dampen antitumor immunity. Among those metabolites is kynurenine (Kyn), which promotes an immunosuppressive TME though inhibiting the activation of effector T cells, while promoting Treg differentiation (39, 40). Kyn is produced as the by-product of tryptophan (Trp) catabolism(41). Indoleamine 2,3-dioxygenase 1 (Ido1) is a rate-limiting enzyme in the Trp catabolism, and often cancer cells show high levels of its expression especially in the advanced stages (42, 43). Traditionally, Ido1 was thought to promote immunosuppressive effect mainly though reducing the levels of Trp, which activates the kinase general control nonderepressible 2 (GCN2). GCN2 is a serine/threonine kinase that phosphorylates eukaryotic initiation factor 2α kinase (eIF2α), which limits the cellular capacity for protein production(42). Activation of GCN2 diminishes the activation and proliferation of T cells and induces T cell anergy and apoptosis(44). Emerging studies showed that Ido1 mediated tumor immune evasion role through the ligand-activated transcription factor aryl hydrocarbon receptor (AhR)(45, 46). Ido1 product Kyn, as well as its downstream metabolic product kynurenic acid, binds to AhR resulting in its activation, which promotes the generation of immune-tolerant DCs, TAM, MDSCs and Tregs fostering an immunosuppressive TME(44, 47, 48).

Within the TME, various immune cell subsets are recruited through interactions between chemokines and chemokine receptors(23). Chemokines are small, secreted proteins that mediate immune cell trafficking and lymphoid tissue development(23, 49). The chemokines are subdivided into four main classes depending on the location of the first two

cysteine (C) residues in their protein sequence: the CC-chemokines, the CXC-chemokines, C-chemokines and CX3C- chemokines(50). In response to specific chemokines, different immune cells migrate into the TME in a spatiotemporal manner. For example, CXCL9, CXCL10 and CXCL11 promote the recruitment of antitumor immune cells such as Th1, NK and CD8 T cells(23, 51). On the other hand, CCL2 and CCL5 promote the recruitment of immunosuppressive cells such as MDSCs(23, 52).

The plasticity of cancer cells requires adaptive transcriptional and post-transcriptional networks that regulate primary tumor progression, metastasis and resistance to therapy. The Arid (AT-rich interaction domain) family contains a DNA-binding domain that was initially found to interact with AT-rich DNA elements(53–55). The Arid family has been found to affect cell growth, differentiation, and development through transcription regulation of different molecules. Recently, extensive studies have suggested tumor promoting or suppressive role of different Arid proteins including Arid1a, Arid1b, Arid3a, Arid4B(55, 56). Although, most of the studies have focused on transcriptional role of Arid proteins, Arid5a has been reported to have both transcriptional and post-transcriptional activities(57–59). Arid5a binds to the 3'-UTR of interleukin-6 (*IL-6*) mRNA via the Arid motif by competing with the *IL-6* mRNA destabilizer Regnase-1(57, 60, 61). Subsequently, Arid5a stabilizes several other mRNAs, including *Stat3*, *T-bet*, and *Ox40*, by binding to their 3'-UTRs(57, 60). Furthermore, Arid5a-deficient mice are resistant to experimental autoimmune encephalomyelitis, bleomycin-induced lung injury, and septic shock(57, 60, 61). However, the role of Arid5a in cancer progression remains unstudied.

A mesenchymal phenotype is the hallmark of tumor aggressiveness in various tumors such as pancreatic and colon cancers(12, 62–67). However, the regulatory programs responsible for implementing the associated molecular signature remain largely unknown. In this study, I investigated the possible role of Arid5a in regulating mesenchymal tumor

progression. By using PDAC and CRC as model for mesenchymal tumors, I revealed that Arid5a is a key molecule for promoting the progression of mesenchymal tumor through promoting their immune evasion. These findings provide new insights towards understanding the roles of Arid5a in the progression of mesenchymal tumor subtypes.

Results

1. Arid5a promotes mesenchymal phenotype in PDAC

Arid5a is expressed in mesenchymal tumor subtypes

To examine the role of Arid5a in tumor, I analyzed the expression of Arid5a in different human pancreatic cancer cell lines spanning epithelial and quasi-mesenchymal (QM) characteristics(65, 68). The HPAF-II and Capan-2 cell lines show epithelial phenotypes, whereas Panc-1 and Mia-PaCa-2 cells have the QM phenotype. BxPC3 and SW1990 cells retain both epithelial and mesenchymal characteristics, resulting in partial epithelial-to-mesenchymal transition (EMT)(19). Mesenchymal-like and partial EMT cell lines showed much higher expression levels of ARID5A than epithelial-like cell lines (**Fig. 1A**). The tumor-intrinsic mesenchymal phenotype has been reported to facilitate immune evasion via crosstalk with stromal immune cells in the TME(30, 35). Notably, among the PDACs, tumor subtypes with QM characteristics are associated with highly aggressive disease(66). Utilizing the RNA sequencing (RNAseq.) dataset from human PDAC patients of Grimmond's group (66), I found that QM and immunogenic PDACs expressed significantly higher levels of the *ARID5A* transcript than the other PDAC subtypes (**Fig. 1B**). Consistently, analysis of The Cancer Genome Atlas (TCGA) RNAseq. dataset of PDAC (https://cancergenome.nih.gov/) demonstrated that *ARID5A* expression significantly correlates with the expression of cytokines associated with EMT induction, such as *TGFB1* and *IL6*, and that of representative EMT-associated transcription factors (EMT-TFs), such as *ZEB1*, *ZEB2*, *SNAI1*, *SNAI2*, *TWIST1*, and *TWIST2* (**Fig. 1C**).

In PDAC, the *KRAS* proto-oncogene and the *TP53* tumor suppressor gene are two of the most commonly mutated genes(69–71). All human PDACs have 80-90% of *KRAS* mutations and deletion in *TP53* in 50–75% of PDACs. Thus, one of the well established genetically engineered mouse models of PDAC incorporates mutations

in *Kras* and *Trp53* that are targeted specifically to the mouse pancreas using Cre-Lox technology(72). Here, I focus on the *LSL-Kras*$^{G12D/+}$*;LSL-Trp53*$^{R172H/+}$*;Pdx-1-Cre* (KPC) mouse model of PDAC as a platform for investigating the role of Arid5a in regulation of mesenchymal tumor subtypes.

TGF-β is a secreting cytokine which act as a tumor suppressor by inducing cytostasis and the apoptosis of normal and premalignant cells(73). However, at later stages, when cancer cells have acquired oncogenic mutations and/or have lost tumor suppressor gene function, such as in PDAC, TGF-β functions as a tumor promotor by stimulating tumor cells to undergo EMT(74). To further investigate the functional role of Arid5a during EMT, I treated KPC cells TGF-β at different time points and found that TGF-β stimulation induced EMT-like morphological changes in KPC cells (**Fig. 1D)**, and under these conditions, promoted the expression of Arid5a (**Fig. 1E**). These results indicate that Arid5a might be involved in the establishment of mesenchymal phenotype of PDAC.

Generation of Arid5a KO KPC cells using CRISPR-Cas9.

To study the possible roles of Arid5a in tumor progression, I generated Arid5a-deficient (KO) KPC cells using the CRISPR/Cas9 mediated gene deletion using two single-guide RNAs (sgRNA). One sgRNA was designed to delete twenty-eight base pairs around the 3'-region of the exon 2, whereas the other sgRNA was designed to delete seventy base pairs around the 3'-region of the exon 5 (**Fig. 2A**). Next, I performed the single cell dilution and validated the deletion of the exon 2 and 5 in two selected clones (KO 4 and 5) by using genomic-PCR analysis (**Fig. 2B**). Moreover, I confirmed the deletion of *Arid5a* at the mRNA and protein levels as measured by qPCR and western blot analysis (**Fig. 2C and D**).

Arid5a plays crucial roles in IL-6- and TGF-β-induced mesenchymal phenotypes of KPC cells

To examine the possible role of Arid5a in promoting mesenchymal phenotype of KPC cells, I performed RNA isolation followed by RNAseq. analysis of WT and KO KPC cells. RNAseq. analysis data demonstrated that EMT-TFs and EMT markers, such as *Zeb1*, *Zeb2*, *Snai1*, *Snai2*, *Twist2*, *Acta2*, and *Itgb1*, were significantly downregulated in KO KPC cells compared with WT cells. On the other hand, the expression of the representative epithelial marker such as E-cadherin (*Cdh1* gene) was substantially increased (**Fig. 3A**). Using Ingenuity Pathway Analysis (IPA), I found that signal pathways associated with EMT and metastasis, such as the regulation of EMT by growth factors/development, IL-8, oncostatin M, and stemness signals, were decreased upon the deletion of *Arid5a* (**Fig. 3B**). In addition, the IL-6, Stat3, and JAK/Stat signaling pathways were downregulated in KO KPC cells (**Fig. 3B**). The activation of the IL-6/JAK/STAT3 signal upregulates EMT-TFs, and enhances metastasis via the induction of EMT(19). These data indicate a possible involvement of Arid5a in inducing the mesenchymal properties of the partial EMT cell lines.

TGF-β and IL-6 are potent EMT inducers in epithelial cell cultures from mammary, lung, pancreatic, and other tissues(75), and is associated with cancer invasion and metastasis(76). To further investigate the functional role of Arid5a during EMT, I treated KPC cells with IL-6 and TGF-β at different time points. Consistent with the hypothesis, IL-6 and TGF-β induced EMT-like morphological changes in KPC cells, which were suppressed upon the deletion of *Arid5a* (**Fig. 3C**). Using immunofluorescence imaging, I found that subcellular localization of E-cadherin at the plasma membrane was disrupted upon IL-6 and TGF-β stimulation in WT KPC cells, while it was restored in the deletion of Arid5a KPC cells (**Fig. 3D**). These results suggest that Arid5a is crucial for IL-6- and TGF-β-induced EMT in KPC cells. To investigate whether Arid5a plays roles in the invasion activity of KPC

cells, I next performed the IL-6-induced Matrigel invasion assay. WT, KO, and Arid5a expressing KO (KO+FL) KPC cells were pre-treated with or without IL-6 for 48hrs and then were subjected to invasion assays in the presence of NIH3T3 conditioned medium, which is well established to be a chemoattractant for this assay **(Fig. 3E)**. IL-6-induced invasion activity of WT KPC cells was significantly decreased with deletion of Arid5a. This result was rescued by Arid5a expression **(Fig. 3F).** To exclude the possibility that the result might be affected by cell growth, I monitored the relative cell growth in WT, KO, and KO+FL KPC cells. The relative growth between three cell lines were comparable **(Fig. 3G).** Taken together, these results suggest that Arid5a is involved in maintenance of mesenchymal phenotype and IL-6-induced invasiveness in PDAC. The mesenchymal phenotype of cancer cells has been reported to facilitate immune evasion via crosstalk with stromal immune cells in the TME(30, 35). Taken in consideration, the tight correlation between mesenchymal phenotype and immune evasion of pancreatic cancer cells, I sought to investigate the functional roles of Arid5a in the immune evasion of pancreatic tumors.

2) Arid5a promotes immune evasion of PDAC.

To explore the biological effect of Arid5a on KPC growth, I performed xenograft experiment. I injected 1 x 10^6 cells subcutaneously in both flanks of either immunocompetent (C57BL/6) mice or immunodeficient (nu/nu BALB/c) mice and monitored tumor growth twice a week for 31 days (**Fig. 4A**). Intriguingly, KO KPC xenografts showed significantly less tumor growth than WT xenografts in C57BL/6 mice, indicating the possible role of Arid5a in tumor progression (**Fig. 4B**). Notably, in nu/nu BALB/c mice, KO KPC tumors showed comparable growth to WT tumors (**Fig. 4C**), indicating that Arid5a promotes PDAC progression in an immune cell-dependent manner. To perform the recovery experiment, I generated two stable cell lines using lentiviral transduction; the reconstitution of Arid5a CDS in KO KPC cells

(Arid5a^{hi} KO) and the reconstitution of Arid domain deleted Arid5a (Arid5a$^{\Delta M}$ KO) (**Fig. 4D)**. I found that Arid5a^{hi} KO cells recovered tumor growth to a comparable level to that of WT cells in C57BL/6 mice, whereas the reconstitution of Arid5a-ΔM (Arid5a$^{\Delta M}$ KO) demonstrated tumor growth comparable to that of KO KPC cells (**Fig. 4E)**. On the other hand, all four cell lines showed similar growth in immunodeficient nu/nu BALB/c mice (**Fig. 4F**). Previous study showed that Arid domain is crucial for the functional activity of Arid5a as a post-transcriptional regulator(58). These results indicate that the Arid domain is important for the immune evasive activity via Arid5a.

3. Arid5a enhances suppressive tumor microenvironment

Deletion of *Arid5a* suppress infiltration of immune suppressive cells and promotes anti-tumor immune cells.

To corroborate the role of *Arid5a* in immune evasion, I analyzed immune cells infiltrating the TME of WT or KO KPC cells. I harvested the tumor after day 24 of xenograft tumor transplantation of WT and KO KPC cells in to 5 weeks old female C57BL/6 mice. Then, I isolated single cells from tumor tissue, and enriched CD45^{+} leukocytes for further analysis of immune population (**Fig. 5A)**. Using these isolated CD45^{+} leukocytes, I performed mass cytometry (Cytometry by Time-Of-Flight: CyTOF) analysis. Characterization and quantification of the expression of 28 surface markers and 8 intracellular markers (6 of which are TFs) spanning a wide range of different immune cells populations demonstrated that the genetic ablation of *Arid5a* in KPC cells promotes an antitumor immune response, as shown by the higher frequency of various anti-tumor immune cells in the TME of KO KPC cells than WT KPC cells (**Fig. 5B and 5C**). Among the infiltrated immune cells, immunosuppressive granulocytic myeloid-derived suppressor cells (gMDSCs), also known as polymorphonuclear MDSCs (32), were much more abundant in the TME of WT KPC cells than in the TME of KO KPC cells (**Fig. 5B).** Furthermore, a larger number of Ki67^{+} actively

proliferating dendritic cells (DCs), natural killer (NK) cells, natural killer T (NKT) cells, and T cells were observed in the KO KPC-derived tumors than WT KPC-derived tumors (**Fig. 5B and 5C**). Furthermore, flow cytometry analysis demonstrated that tumor-infiltrating gMDSCs were significantly decreased in the TME of KO KPC cells confirming the results from CyTOF (**Fig. 5D and 5E**). These findings suggested that Arid5a facilitates the immune evasion of PDAC by promoting the intratumoral infiltration of suppressive immune gMDSCs and suppression of anti-tumor immune cells.

Arid5a suppress effector T cells infiltration and promotes T-cells exhaustion in the TME.

Global analysis demonstrated that numerous clusters of T cells were substantially expanded upon the deletion of *Arid5a,* including effector memory (EM) ($CD44^{+}CD62L^{-}$) $CD4^{+}$ T cells, central memory (CM) ($CD44^{+}CD62L^{+}$) $CD8^{+}$ T cells, and EM ($CD44^{+}CD62L^{-}$) $CD8^{+}$ T cells (**Fig. 6A and 6B**). The in-depth analysis of the $CD4^{+}$ and $CD8^{+}$ T-cell compartments showed that the exhausted PD-1^{hi}Tbet^{+} EM Th1 cell population was significantly decreased in the TME of KO KPC cells, and this PD-1^{hi} cell population was replaced by PD-1^{int} and PD-1^{lo} EM Th1 cells in the TME of KO KPC cells (**Fig. 6A and 6B**). Consistent with the supportive role of Arid5a in immunosuppression, I found that activated $KLRG1^{+}$ Tregs were significantly reduced in the TME of KO KPC cells compared with WT KPC cells (**Fig. 6A and 6B**). Similar to $CD4^{+}$ T cells, the number of PD-1^{hi}LAG$3^{hi}CD39^{+}$ $CD8^{+}$ T EM subset cells with an exhaustion-like phenotype was significantly decreased in the TME of KO KPC cells compared with WT KPC cells (**Fig. 6C and 6D**). Furthermore, flow cytometry analysis demonstrated that tumor-infiltrating Tregs were significantly decreased in the TME of KO KPC cells confirming the results from CyTOF (**Fig. 6E and 6F**) These findings suggested that Arid5a promotes infiltration of Tregs and exhausted T lymphocytes in PDAC.

Deletion of *Arid5a* induces the cytotoxic activity of tumor-infiltrating T cells

To further characterize the cytotoxic activity of $CD4^+$ and $CD8^+$ T cells, I analyzed the production of granzyme B (GzmB) and interferon-gamma (IFN-γ) in tumor infiltrating T cells (**Fig. 7**). I stimulated tumor infiltrating $CD45^+$ leukocytes with PMA/ionomycin ex vivo for 3 h and applied for flow cytometry analysis. The analysis of TILs demonstrated that $CD8^+$ T cells were significantly upregulated (**Fig. 8A.a**) and $CD4^+$ T cells were reciprocally decreased upon the deletion of Arid5a in KPC cells (**Fig. 8A.b**). Infiltrating effector $CD8^+$ T cells of KO KPC tumors expressed significantly higher levels of GzmB compared with TILs of WT cells (**Fig. 8B**), and infiltrating effector $CD4^+$ T cells among KO KPC cells also showed a similar trend (**Fig. 8C and 8D**). Concurrently, both infiltrating effector $CD4^+$ and $CD8^+$ T cells in KO KPC tumors significantly induced the production of IFN-γ, a potent anti-tumor cytokine (**Fig. 8E and 8F**). Taken together, these results indicated that *Arid5a* suppresses the cytotoxic activity of $CD4^+$ and $CD8^+$ T cells in WT KPC TME.

4. Arid5a promotes tryptophan metabolism in KPC cells

Arid5a promotes IFN-γ-induced Ido1 expression but not pStat1 in KPC cells.

I next sought to identify the molecular mechanisms underlying how Arid5a promotes the immune evasion of PDAC. Comparing the gene expression profiles of KO and WT KPC cells by RNAseq. analysis showed diminished expression levels of the genes associated with inflammation and immune evasion such as *Ido1*, *Ido2, Adora2a*, and chemokines, in KO compared to WT KPC cells (**Fig. 9A**). The Ingenuity Pathway Analysis software (IPA) analysis showed that the deletion of *Arid5a* decreased canonical signaling pathways associated with the hepatic fibrosis signal, proinflammatory response (NF-κB, IL-1, IL-6, acute phase response), cell proliferation, invasion (Stat3, P13K/AKT, ERK/MAPK, PDGF),

and tryptophan degradation III. In contrast, tumor suppressor PTEN signaling was increased in KO KPC cells (**Fig. 9B**).

Increased levels of *Ido1* in both mouse and human tumor models is responsible for the tumor immune evasion process(42, 43). Analysis of TCGA RNAseq. dataset of PDAC showed a positive correlation of *ARID5A* with *IDO1* and the significant association of IDO1 with a poor prognosis in human pancreatic cancers (**Fig. 9C and 9D**). These results highlight *Ido1* as a possible downstream target of *Arid5a* in the immune evasion of pancreatic tumors. Ido1 expression in the TME promotes tumorigenesis via the induction of numerous tolerogenic immune phenotypes, such as the suppression of effector T-cell activation and the enhanced infiltration of Tregs and MDSCs(32, 42, 77). The enzyme Ido1, which is upregulated by IFN-γ, promotes Kyn production by catalyzing the amino acid Trp(45). Upon IFN-γ stimulation, KPC cells expressed both *Ido1* mRNA and protein, which were significantly decreased upon the deletion of *Arid5a* (**Fig. 9E and 9F)**. Unlike IFN-γ, IFN-α and IFN-β did not induce the expression of *Ido1* in KPC cells (**Fig. 9G).**

IFN-γ-mediated JAK–Stat1 signaling activates *Ido1* transcription(45, 78). The expression kinetics of Tyr^{701}-phosphorylated Stat1 (pYStat1) and Stat1 were comparable between WT and KO KPC cells (**Fig. 9H**). Furthermore, the silencing of Stat1 expression substantially reduced Ido1 expression, but did not affect Arid5a expression (**Fig. 9I and 9J**). Taken together, these results indicate that pYStat1 might activate the initial transcription of *Ido1,* followed by the post-transcriptional stabilization of *Ido1* mRNA by Arid5a in KPC cells.

Tryptophan metabolites are decreased upon deletion of *Arid5a.*

Ido1 inhibits the activation of effector T cells through depletion of the essential amino acid tryptophan (Trp), and promotes Treg differentiation and activation through Kyn

production(42, 43, 45). I next analyzed Kyn as the downstream molecule of Ido1. Consequently, KO KPC cells stimulated with IFN-γ released significantly smaller amounts of Kyn into the supernatant than WT cells at 48 h as measured by ELISA (**Fig. 10A**). Next, I isolated WT and KO xenograft KPC tumor at day 10 and day 21 after inoculation and I performed liquid chromatography coupled to tandem mass spectrometry (LC-MS/MS) to analyze Arid5a induced tryptophan metabolism *in vivo.* LC-MS/MS analysis showed that Kyn levels were significantly decreased in both the sera and tumors of mice 10 days after inoculation with KO KPC cells (**Fig. 10B)**. On day 21, Kyn production was significantly decreased in the serum, and showed a decreasing tendency in KO KPC tumors (**Fig. 10C**). The production of kynurenic acid, a downstream metabolite of Kyn, was significantly suppressed in the tumors of mice with KO KPC xenografts on day 10 and 21, but not in their sera (**Fig. 10D**). Similarly, Trp levels were significantly increased in KO KPC tumors on day 21 (**Fig. 10E**). Collectively, these results suggest that Arid5a regulates Ido1-mediated Trp metabolism in KPC cells.

Arid5a stabilizes Ido1 mRNA by binding to its 3'-UTR.

Arid5a promotes the inflammatory response underlying various diseases through stabilization of the mRNAs of several genes, such as *IL6*, *Stat3*, *T-bet*, and IL17-induced targets, and contributes to the inflammatory response and a variety of diseases(57, 60). Therefore, I tested whether Arid5a promotes Ido1 expression through stabilizing its mRNA. In this study, I performed RNA stability assay using actinomycin D. I treated WT and KO KPC cells with IFN-γ for 6 h to induce the transcription of Ido1. Then, I treated WT and KO KPC cells with actinomycin D to inhibit the transcription of Ido1 followed by RNA isolation at different time points. I found that IFN-γ treated KO KPC cells showed a significantly decreased half-life of *Ido1* mRNA after actinomycin D treatment compared with WT cells (**Fig. 11A**). Then I

generated a luciferase vector encoding the 3′-UTR region of *Ido1,* to determine whether Arid5a stabilizes *Ido1* mRNA. Analysis of the luciferase activity of *Ido1* through transient expression of Flag-tagged full-length Arid5a (Arid5a-FL), Arid5a-ΔM, or an empty vector in KO KPC cells showed that Arid5a stabilizes *Ido1* mRNA **(Fig. 11B and 11C**). To determine the direct binding of Arid5a to *Ido1* mRNA, I first prepared modified RNAs of 3'-UTR of *Ido1* or mock control using by 5-bromo-UTP (BrU) through *in vitro* transcription (**Fig. 12D)**. Then, I immunoprecipitated RNA-binding proteins using anti-BrU antibody, conjugated with magnetic beads, and found that Arid5a binds directly to *Ido1* mRNA **(Fig. 12E**). These data show that Arid5a binds to and stabilize *Ido1* mRNA binding to its 3'-UTR.

Arid5a promotes tumor growth partially through Ido1-Kyn axis

To investigate the *in vivo* biological role of the Arid5a-mediated Ido1-Kyn axis, I generated two stable cell lines using lentiviral transduction; *Ido1* knockdown KPC cells (shIdo1) and Ido1-expressing KO KPC cells ($Ido1^{hi}$ KO cells) (**Fig. 12A and 12B).** I found that mice inoculated with shIdo1 KPC cells showed suppressed tumor growth compared with mice inoculated with WT cells (**Fig. 12C**). Consistent with the role of Ido1 as a downstream regulator of Arid5a, $Ido1^{hi}$ KO KPC cells partially recapitulated the growth of KO KPC cells (**Fig. 12E**). Intriguingly, $Ido1^{hi}$ KO KPC did not fully recover the tumor growth of KO KPC cells, indicating that Arid5a regulates KPC growth through other downstream targets beside that of Ido1 (**Fig. 12E**). In contrast, nu/nu BALB/c mice showed comparable tumor growth when inoculated with either WT or KO KPC cells (**Fig. 12D and 12F**). These results demonstrate that Arid5a-mediated tumor growth in KPC cells is partially regulated through Ido1-mediated Trp metabolism.

5. Arid5a promotes chemokine expression which facilitates immunosuppressive tumor microenvironments.

***ARID5A* correlates with chemokines expression in PDAC patients**

Tumor cells and stromal cells in the TME produce various chemokines which recruits different immune cell subsets into the TME(15, 23). To test whether chemokine signaling is involved in Arid5a-mediated immune evasion, I analyzed the TCGA dataset of human pancreatic cancer. I found that multiple chemokines, including *CCL2*, *CCL5*, *CCL7*, and *CCL8* positively correlated with *ARID5A* expression (**Fig. 13A**). My RNAseq. data showed that *Ccl2*, *Ccl5*, *Ccl7*, *Ccl8*, and *Cxcl3* expression was decreased in KO as compared to WT cells (**Fig. 9A**). I confirmed these data using qPCR (**Fig. 13B**). Importantly, KPC cells expressed the *Ccl2* transcript predominantly compared with other chemokines (**Fig. 13C)**. Consistently, the protein levels of Ccl2 in KO KPC cell supernatants were significantly lower than in WT cells (**Fig. 13D)**. Taken together, Arid5a correlates with *CCL2* in PDAC and promotes Ccl2 expression in KPC cells.

Arid5a binds to 3'-UTR and stabilize Ccl2 mRNA

An increased level of CCL2 was shown to be a poor prognostic indicator in patients with PDAC (79). In addition, to date, the pivotal roles of Ccl2 in MDSC recruitment and tumor progression have been reported in CRC, glioma, renal cancer, lung cancer, liver cancer, and melanoma models (23, 52), but not in pancreatic cancer. Furthermore, it has been demonstrated that MDSCs mediated Treg development via TGF-β and IL-10 production in the TME (36). Thus, a high *Ccl2* expression level in KPC cells compared with other chemokines, its prognostic implications, and its immune suppressive effects prompted us to analyze the role of Arid5a in regulating Ccl2. Arid5a was able to stabilize *Ccl2* mRNA, as measured by luciferase activity **(Fig. 14A**). To determine the direct binding of Arid5a to *Ccl2*

mRNA by RNA pulldown, I prepared BrU-labeled RNAs, as mentioned (**Fig. 14B)**. Then, I immunoprecipitated RNA-binding proteins using the anti-BrU antibody, and found that Arid5a binds directly to *Ccl2* mRNA **(Fig. 14C**). Collectively, Arid5a stabilizes *Ccl2* mRNA binding to its 3'-UTR.

Arid5a augments tumor growth through enhancing Ccl2 production

To investigate the biological role of Arid5a-mediated *Ccl2* stabilization in KPC tumor growth *in vivo*, I generated 2 stable cell lines using lentiviral transduction; Ccl2 knockdown KPC cells (shCcl2) and Ccl2-expressing KO KPC cells ($Ccl2^{hi}$ KO) (**Fig. 15A and 15B**). I inoculated these cell lines subcutaneously into the immunocompetent and immunodeficient mice, and measured the tumor growth. I found that shCcl2 KPC cells showed reduced tumor growth in immunocompetent mice compared with WT KPC cells (**Fig. 15C**). Of note, the rate of tumor growth of $Ccl2^{hi}$ KO KPC cells was similar to that of WT cells in immunocompetent mice (**Fig. 15E**). In contrast, shCcl2 and $Ccl2^{hi}$ KO KPC tumor growth was comparable to WT tumor growth in immunodeficient mice (**Fig. 15D and 15F**). Taken together, the post-transcriptional stabilization of *Ccl2* mRNA is a common mechanism controlling Arid5a-mediated tumor progression.

6. Arid5a promotes immune evasion in mesenchymal colorectal tumors

Arid5a is expressed mesenchymal tumor subtypes colorectal tumors

I next sought to determine whether these above findings reflect a general mechanism common to other mesenchymal tumor subtypes. I performed immunoblotting analyses to investigate the expression of ARID5A in human CRC cell lines, including DLD1, Caco-2, LS174T, HCT116, SW480, and SW620. Consistent with PDAC, CRC cell lines with a partial-EMT phenotype, namely, HCT116, SW480, and SW620 cells, expressed high levels

of the ARID5A protein (**Fig. 16A**). Similarly, Guinney and colleagues recently identified 4 robust consensus molecular subtypes (CMSs), using a total of 18 CRC datasets (n = 4,151 patients) (80). I analyzed their RNAseq. dataset and found that cells with CMS4, a mesenchymal subtype, expressed significantly higher levels of *ARID5A* than the other subtypes (**Fig. 16B**). Similar to PDAC, analysis of the TCGA dataset of CRC demonstrated that *ARID5A* expression is weakly but significantly correlated with the expression of *TGFB1*, *IL6*, and representative EMT-TFs including *Zeb1, Zeb2, Snai1, Snai2* (**Fig. 16C**).

Arid5a is involved in immune evasion of colorectal cancer.

Furthermore, to investigate whether Arid5a is involved in the immune evasiveness of CRC, I used a highly metastatic CRC mouse model MC38 (81, 82), in which tumors show extensive infiltration of immunosuppressive cells, such as MDSCs, whereas they show the exclusion of T cells (26, 83). To investigate the role of Arid5a in MC38 tumor progression, KO MC38 cells was generated using CRISPR/Cas9 (**Fig. 17A**). Deletion of Arid5a in MC38 cells was confirmed in mRNA and protein expression (**Fig. 17B,** and **17C**). When I inoculated WT and KO MC38 cells subcutaneously, KO tumor showed remarkably reduced growth in syngeneic mice, but not in immunodeficient mice as compared to WT MC38 cells (**Fig. 17D and 17E**). These results indicate that similar to PDAC, *Arid5a* does not play a crucial intrinsic role in MC38 tumor growth *in vivo,* but might be involved in the immune evasion of MC38 tumor.

Arid5a promotes immune suppressive TME in MC38 tumor.

Next, to monitor the infiltration of immune cells in TME, I isolated tumor infiltrating $CD45^+$ leukocytes from the WT and KO MC38 tumors at day 14 of subcutaneous MC38 cells inoculation. Then, I performed CyTOF using isolated $CD45^+$ leukocytes. Consistent with PDAC, I found that immunosuppressive MDSC subsets, mainly gMDSCs, were suppressed

(**Fig. 18A)**, whereas immunocytes, such as DCs, NK, NKT, CM $CD8^+$, EM $CD8^+$, and EM $CD4^+$ T cells were expanded in KO MC38 tumors, indicating the activation of anti-tumor immune responses in mice upon the deletion of *Arid5a* in inoculated tumors (**Fig. 18A and 18B**). Similarly, KLRG1 and CD44-expressing intratumoral $CD103^+$-activated Treg subsets were significantly reduced, similar to activated Tregs in the microenvironment of KO KPC tumors (**Fig. 18C and 18D)**. The subsets of T-bet^+ EM cells were significantly increased in KO MC38 tumors showing an upregulation of $CD4^+$ T cells with effector-like phenotypes. On the other hand, naïve ($CD62^+CD44^-$) $CD4^+$ T-cell subsets were expanded in KO MC38 tumors, likely owing to the differentiation process of naïve $CD4^+$ T cells into multiple effector subsets that can mediate various types of antitumor immunity (84) (**Fig. 18C and 18D)**. EM cells circulate through tumor tissues and are known to have cytotoxic properties (85). Infiltration of the $Ly6C^+$ $PD1^{hi}$ EM subset of $CD8^+$ T cells with an effector-like phenotype was upregulated in KO MC38 tumors (**Fig. 18E and 18F**). However, the expansion of naïve $CD8^+$ T cells was downregulated upon *Arid5a* deletion, indicating that naïve cells might have differentiated into EM subsets. These results suggest the general roles of Arid5a in promoting tumor immune evasion through disrupting the balance between immunosuppressive and antitumor immune cells in the TME.

Arid5a corelates with chemokines and promotes Ccl2 expression in MC38 cells.

To understand the common underlying mechanism regulated by Arid5a, I monitored the expression of Ido1 and chemokines in WT and KO MC38 cells. In contrast to a previous report (86), IFN-γ-induced Ido1 protein expression was not detected in MC38 tumors (**Fig. 19A**). Analysis of the TCGA RNAseq. dataset of CRC demonstrated that ARID5A expression correlated with expression of chemokine transcripts, such as *CCL2*, *CCL5*, *CCL7*, and *CCL8* **(Fig. 19B**), which was supported by the RNAseq. data of WT and KO MC38 cells **(Fig. 19C**). Similar to KPC cells, *Ccl2* expression was markedly decreased in KO MC38 cells

compared with the other chemokines (**Fig. 19C and 19D**). In addition, WT MC38 cells expressed higher levels of *Ccl2* than the other chemokines (**Fig. 19E)**, indicating *Ccl2* as a possible downstream target of Arid5a. Consistently, protein levels of Ccl2 in WT MC38 cell supernatants were significantly higher than those in KO MC38 cells (**Fig. 19F)**. Similar to PDAC, flow cytometry analysis of TILs in MC38 tumor showed significantly lower infiltration of gMDSCs (**Fig. 19G**). Taken together, Arid5a promotes Ccl2 expression in MC38 cells to create immunosuppressive TME.

Arid5a promotes tumor growth in MC38 cells through Ccl2 production.

To investigate the importance of Arid5a-Ccl2 axis in regulation of tumor growth *in vivo*, I knock down Ccl2 using different clones. generated 4 stable cell lines using lentiviral transduction; i.e., MC38 KO cells expressing Arid5a-FL (Arid5a^{hi} KO), Arid5a-ΔM (Arid5a$^{\Delta M}$ KO), or Ccl2 (Ccl2^{hi} KO), and Ccl2 knockdown MC38 cells (shCcl2). Before using shCcl2 clone for lentiviral transduction, I transiently transfected shCcl2 to monitor the knock down efficiency of different clones. I found that all five clones effectively suppressed Ccl2 expression as measured by qPCR (**Fig. 20A)**. Then, I used shCcl2-1 (shCcl2) for lentiviral transduction. I found that the inoculation of KO MC38, Arid5a$^{\Delta M}$ KO, and shCcl2 cells into immunocompetent mice showed suppressed tumor growth compared with the inoculation of WT cells (**Fig. 20B**). Notably, the rate of tumor growth was a similar level to that of WT cells in MC38 Arid5a^{hi} KO and Ccl2^{hi} KO cells (**Fig. 20B**). By contrast, in immunodeficient mice, tumors derived from all of our generated MC38 cell lines showed comparable growth to WT tumors (**Fig. 20C**). Thus, Arid5a promotes the immune evasion of MC38 tumors through the regulation of *Ccl2* transcripts. These results suggest that the post-transcriptional stabilization of *Ccl2* mRNA is a common mechanism controlling Arid5a-mediated immune-evasive tumor progression.

Discussion

Harnessing the power of immune cells highlights an important step towards treating wide range of cancers, which is currently known as cancer immunotherapy(30, 87). For decades, scientific efforts to dissect the mechanisms of immune evasion of tumor cells have primarily focused on immune checkpoint blockade through immune checkpoint inhibitors (ICIs)(35, 88). However, the anti-tumor response of the currently available ICIs for mesenchymal tumors has not been satisfactory(89). Moreover, late diagnosis of mesenchymal tumors represents a limiting factor in their eradication. Therefore, understanding the mechanisms regulating the acquisition of mesenchymal phenotype in tumors might reveal novel pharmacologically targeted molecules for better immunotherapy modalities. By using unbiased genotypic and phenotypic profiling of the mesenchymal TME, I unraveled a novel dual role of Arid5a as a key molecule for mesenchymal tumor progression.

Establishing a mesenchymal phenotype is a key step for invasion and metastasis during tumors progression(74, 90). TGF-β and IL-6 induce the mesenchymal phenotype of a wide range of tumors such as mammary, lung, pancreas(65, 75, 91), and is associated with cancer invasion and metastasis(76, 92). Using pancreatic and colorectal cancer as model for mesenchymal tumors, I found that Arid5a is crucial for the establishment of the mesenchymal phenotype of cancer. Three lines of evidence supported my conclusion. First, Arid5a is expressed exclusively in pancreatic and colorectal cancer cell lines representing EMT or mesenchymal phenotypes such as Panc-1 and SW620 cells, respectively. In contrast, Arid5a is not expressed in pancreatic and colorectal cancer cell lines of epithelial origin such as HPAF-II and DLD-1 cell lines. Second, genetic ablation of Arid5a in mesenchymal pancreatic cancer cell lines abolished the TGF-β and IL-6—induced mesenchymal phenotype. Third, the deletion of Arid5a suppressed the IL-6 induced invasion activity in KPC cells which was rescued with forced expression of Arid5a in KO cells.

Tumors develop within complex tissue environment consisting of diverse immune cells, stromal cells, vascular networks and secreted molecules(15). Main challenge in cancer research is to identify the major factor contributing in the tumor growth so as to develop treatment strategies(14, 89). In this regard, my finding showed that genetic ablation of *Arid5a* in PDAC and CRC abolished tumor growth compared to WT tumor in immunocompetent mice. In contrast, *Arid5a* deficient PDAC and CRC showed comparable tumor growth compared to WT tumor in immunodeficient mice. The simplest interpretation of these observations is that Arid5a promotes immune evasion of mesenchymal tumors.

Tumors are dichotomized into hot or cold based on their level of T cell infiltration and molecular signatures of immune activation in immune landscape of TME(93). Mesenchymal tumors such as PDAC and CRC, based on abundant presence of suppressive immune cells, are characterized by an immunologically "cold" TME and are usually referred to as non-T-cell inflamed tumors(22, 28). In addition, prognostic analyses of tumor-infiltrating immune cells show that infiltration of $CD8^+$ T, Th1, Tfh, B, and NK cells, and DCs into a tumor is associated with a favorable prognosis in most cancers(30, 93). Consistent with these premises, phenotypic profiling of the immune cells infiltrating the TME of PDAC and CRC tumors showed high infiltration of immunosuppressive immune cells on the expense of tumor fighting immune cells, which is characteristic of the immunologically cold TME of mesenchymal tumors. Intriguingly, genetic ablation of *Arid5a* in PDAC and CRC resulted in immunologically hot TME attributed to the high infiltration and functionality of anti-tumor immune cells. Four independent pieces of evidence supported my findings. First, with deletion of Arid5a, TME of PDAC and CRC were less suppressive as demonstrated by diminished infiltration of gMDSCs and Tregs as compared to WT tumors. Second, in the global analysis of TIL, infiltration of antitumor immune cells, such as DCs, NK, NKT, and T cells, was increased in Arid5a deficient TME compared to WT. Third, infiltrated immune

cells in Arid5a deleted tumors were more activated and less exhausted as shown by decreased infiltration of Ly6C^{-}PD1^{hi} EM CD8^{+} T cells compared to WT tumors. Fourth, T cell infiltrating Arid5a deficient tumors showed higher cytotoxic abilities as manifested by increased Tbet^{+} EM CD4^{+} T-cell population and increased secretion of IFNγ and GzmB by both CD4^{+} and CD8^{+} T cells. Thus, my findings support a crucial role of Arid5a in promoting the immune evasion of mesenchymal tumors through maintaining an immunosuppressive TME.

Understanding the interplay between tumor cells and TILs within the TME holds great therapeutic potential(15, 30). Targeting the metabolic cues may remodel the TME for effective and durable antitumor T cell immunity. Therapeutically targeting the Ido1– Kyn–AhR signaling pathway may offer potentially novel anticancer modalities. The first-generation Ido1 inhibitors, exemplified by indoximod and epacadostat did not show significant antitumor activity as monotherapy in patients with advanced cancers(94). However, durable responses have been reported for combined therapy between epacadostat with the PD-1 immune checkpoint inhibitor pembrolizumab(42, 95). In addition, direct and indirect exploiting of chemokine–chemokine receptor signaling pathways may remodel the immune and biological phenotypes of a tumor(35, 79). However, clinical trials of agents targeting a single chemokine or chemokine receptor in chronic inflammatory diseases were not promising(23). Therefore, it is predicted that chemokine targeting my not offer good antitumor therapy(96). Nevertheless, it may achieve clinical benefits in combination with other immune therapy modalities(97, 98). Based on these clinical trials, targeting multiple pathways within the TME is predicted to offer effective and durable antitumor therapy(35, 79, 97, 99). Consistent with this notion, I found that Arid5a deficient tumors showed diminished tumor growth compared to Ido1 deficient cells as demonstrated by the growth of KPC cells *in*

vivo. This can be attributed to the role of Arid5a in regulating chemokines production such as Ccl2 beside that of promoting Ido1 expression.

Mechanistically, I found that Arid5a promotes the expression of Ido1 and Ccl2 through posttranscriptional stabilization of their 3'UTRs. Three independent experimental approaches supported my conclusion. First, the expression of Ido1 and Ccl2 was diminished in Arid5a deficient PDAC and CRC compared to WT cells. Second, Arid5a promotes the stability of the 3'UTR of Ido1 and Ccl2 as measured by luciferase activity. Third, Arid5a physically bound 3'UTR of Ido1 and Ccl2 as shown by Ribotrap assay. Thus, my study highlights the importance of posttranscriptional regulation in shaping mesenchymal tumor growth and immune evasion.

In sum, my study unravels Arid5a as a key molecule in orchestrating the immune evasion of mesenchymal tumors such as PDAC and CRC. Arid5a executes dual roles to promote the immune evasion; a metabolic role through promoting the Ido-Kyn-AhR signaling axis, and an immunomodulatory role through enhancing Ccl2–Ccr2 signaling. Thus, therapeutic targeting of Arid5a in mesenchymal tumors may provide a potential treatment modality either as monotherapy or in combination with other immunotherapy modalities.

Materials and methods

Mice

C57BL/6 mice and nu/nu BALB/c mice were purchased from CLEA Japan. All experiments were performed in accordance with the guidelines approved by the Animal Care and Use Committees of Immunology Frontier Research Center and the Research Institute for Microbial Diseases, Osaka University.

Cell Lines

HPAF-II, Capan-2, BxPC-3, Panc-1, Mia-PaCa-2, SW1990, DLD1, Caco-2, LS174T, HCT116, SW480, and SW620 cells were from the American Type Culture Collection. Mia-PaCa-2, Panc-1, Caco-2, LS174T, HCT116, SW480, and SW620 cells were cultured in DMEM (Nacalai, cat. #08456-36) containing 10% (vol/vol) fetal calf serum (FCS) (HyClone, cat. #SH30071.03); BxPC-3, SW1990 and DLD1, cells were cultured in RPMI 1640 medium (Nacalai, cat. #30264-56) containing 10% (vol/vol) FCS; Capan-2 cells were cultured in McCoy's 5a medium (Sigma, cat. #M9309) containing 10% (vol/vol) FCS; and HPAF-II cells were cultured in Minimum Essential Media (MEM) (Gibco, cat. #11095080) containing 10% (vol/vol) FCS. KPC cells were prepared from a Pdx1-cre; LSL-KrasG12D; LSL-Trp53R172H mouse (100), as described previously (101), and cultured in Dulbecco's Modified Eagle Medium (DMEM) medium containing 10% (vol/vol) FCS. MC38 cells were purchased from Kerafast and cultured in DMEM containing 10% (vol/vol) FCS and supplemented with 2mM glutamine (Gibco, cat. #25030081), 0.1 mM nonessential amino acids (Gibco, cat. #11140050), 1 mM sodium pyruvate (Gibco, cat. #11360070), and 10 mM HEPES (Nacalai, cat. #17557-94). 293FT cells were from Invitrogen (cat. #R70007) and were cultured according to the manufacturer's instructions. Plat-E cells were a gift from Dr. Kitamura (Tokyo University), they were cultured in DMEM containing 10% (vol/vol) FCS.

All cell lines used in the experiments were obtained from 2012–2020. Cell viabilities were measured using Cell Counting Kit-8 (CCK-8) (Dojindo, cat. #CK04), according to the manufacturer's instructions. In brief, 96-well plate was pre-incubated for 24 h in humidified incubator and 100 μl of cell suspension (5000 cells/well) were added in a well of the pre-incubated 96-well plate. After incubation for 24 - 48 h, 10 μl of CCK-8 solution was added to each plate followed by incubation for 1-2 h. Then, absorbance at 450 nm was measured using a microplate reader. All cells used were determined to be free of mycoplasma using 4′,6-diamidino-2-phenylindole (DAPI, Sigma-Aldrich, cat. #D9542) before starting the experiments, and no antibiotics were added to the cell cultures throughout the experiments to avoid the latent infection of mycoplasma. All cell lines used in this study were cultured for less than one month for the experiments described.

CRISPR/Cas9 gene editing

To generate *Arid5a*-knockout (KO) cells, KPC and MC38 cells were transfected with one of three plasmids from Santa Cruz—Arid5a/Mrf-1 CRISPR/Cas9 (cat. #sc-431969), Arid5a/Mrf-1 HDR (cat. #sc-431969-HDR), or control CRISPR/Cas9 (cat. #sc-418922)—using UltraCruz® Transfection Reagent (Santa Cruz, cat. #sc-395739) according to the manufacturer's instructions. Briefly, 2 x 10^5 KPC or MC38 cells were cultured in 6-well tissue culture plate in 3 ml of DMEM medium containing 10% (vol/vol) FCS and incubated for 24 h. Solution A was prepared by diluting 1-3 μg of Arid5a/Mrf-1 CRISPR/Cas9 plasmid DNA into 150 μl of plasmid transfection medium (cat. #sc-108062) and mixture was incubated for 5 min in room temperature (RT) after gentle mixing. The solution B was prepared by diluting 5-15 μl of the transfection reagent (cat. #Sc-395739) in 150 μl of plasmid transfection medium and mixture was incubated for 5 min in RT after gentle mixing. After dropwise addition of solution A into solution B, mixture was vortexed immediately and

incubated for 20 min at RT. Then, the mixture was added to each well drop wise. Two days after transfection, cells were cloned by limiting dilution in 96-well plates and single-cell clones were selected and analyzed by genomic PCR to verify *Arid5a* coding sequence integrity. Arid5a depletion was confirmed by quantitative PCR (qPCR) and immunoblotting.

Genomic PCR

DNeasy Blood and tissue kit, Qiagen (cat. #69506) was used to isolate total DNA from WT and KO cells (KPC and MC38). Cultured cells (1-2 x 10^6) were washed and collected in 200 µl PBS, followed by addition of 20 µl proteinase K. 200 µl of buffer AL (provided in the kit) was added in the sample and incubated at 56 °C for 10 min. For the precipitation of DNA, 200 µl was added to the sample and mixed thoroughly and transferred to DNeasy Mini spin column placed in a 2 ml collection tube (provided in the kit). Spin column was centrifuged for 1 min for 8000 rpm and the flow through was discarded, followed by washing of spin column with buffer AW1 and AW2 respectively. The spin column was transferred to new 1.5 ml microcentrifuge tube and 50-100 µl of elution buffer AE was added to the spin column and centrifuged for 1 min for 8000 rpm for elution. The eluted DNA was measured and KOD FX (Toyobo) was used according to manufacturer's protocol for genomic PCR. PCR condition was performed at 98 °C for 10s, 60 °C for 30s followed by 30 cycles and 68 °C for 3 min. Primers used in the experiments are as follows: Arid5a exon 2 Forward: 5'-cctttcccagcagcacctc-3', Arid5a exon 2 Reverse: 5'-tctggctcctgctctgctcat-3', Arid5a exon 5 Forward: 5'-gtcccatggccagagggtg-3', and Arid5a exon 5 Reverse: 5'-ctatgggcagccggctgtac-3'. All oligos were purchased from Thermo Fisher Scientific.

Tumor transplantation experiments

Mouse xenograft experiments were performed as previously published (101). Briefly, KPC (2 x 10^5) or MC38 cells (1 x 10^5) in 100 mL of 50% Growth Factor Reduced BD Matrigel Matrix (BD Bioscience, cat. #354230) were injected into both flanks of either nu/nu BALB/c mice (8- to 10-week-old females) or C57BL/6 mice (8- to 10-week-old females). Tumor growth was measured twice a week for three to four weeks. Tumor volume was calculated using the formula, volume = $(a \times b^2)/2$, in which a and b are the largest and the smallest tumor diameters, respectively.

Tissue processing

Tumors were dissected from the skin of mice at the designated time points and chopped into smaller fragments. The tumor fragments were then transferred to gentleMACS C tubes (Miltneyi Biotec, cat. # 130-093-237) containing 2.5 mL of tumor dissociation enzyme solution (Mouse Tumor Dissociation Kit, Miltneyi Biotec, cat. #130-096-730). Tubes were processed on gentleMACS octo-Dissociator (Miltenyi Biotec, cat. #130-095-937) using the 37°C_mTDK_2 protocol designated for hard tumor tissue. Before further procedures, cell suspensions were filtered using 40 μm cell strainers (Falcon, Corning brand, cat. #352340) and were centrifuged at 500 *g* for 10 min at 4°C. The pellets were then resuspended in 8 mL of 40% Percoll (GE Healthcare, cat. #17-5445-01) and centrifuged at 500 *g* for 10 min at 4°C. Supernatants were aspirated, and cell pellets were quenched with 10 mL RPMI containing 10% FBS, and used for subsequent analyses.

MACS enrichment of $CD45^+$ lymphocytes

For the enrichment of $CD45^+$ leukocytes, single cells isolated from tumor tissues were suspended in 400 μl of FACS buffer (PBS +2% FBS). Then, 40 μl of $CD45^+$ (TIL) MicroBeads, mouse (Miltenyi Biotec, cat. #130-110-618) were added into the cell suspension.

The samples were incubated at 4°C for 15 min, then the cells were washed and resuspended in 2 mL of FACS buffer. The autoMACS Pro Separator (Miltenyi Biotec, cat. #130-092-545) was used to isolate $CD45^+$ leukocytes using "Posssel" program.

Mass cytometry antibodies

Antibodies were conjugated to all metals other than platinum using the MaxPar conjugation kit, cat. #2011698 according to the manufacturer's instructions. Platinum-labelled antibodies were conjugated with cisplatin as previously described (102). Briefly, 50 µg antibody was diluted or reconstituted in R buffer (Fluidigm) to achieve an antibody solution of at least 50% (vol/vol) R buffer. The antibody was concentrated using a 30 kDa spin filter (EMD Millipore, Billerica, MA, cat. #MRCF0R030). A total of 100 µL of a 4 mM tris(2-carboxyethyl) phosphine (TCEP) solution (Thermoscientific, cat. #77720) diluted in R buffer from a 500 mM stock solution was added to the antibody, mixed by pipetting, and incubated in the spin column for 30 min in a 37°C water bath. Then, antibody was washed twice, with 300 and 400 µL C buffer (Fluidigm), respectively. A total of 20 nmol (20 µL of a 1 mM solution in DMSO) cisplatin was thawed and added to the antibody, mixed by pipetting and incubated for 60–90 min in a 37°C water bath, analogous to the MaxPar procedure. The amount of cisplatin used was guided by the approx. 20 nmol of polymer used in one reaction of a MaxPar labeling kit. The utility of that concentration was confirmed by a respective titration experiment.

Metal isotopes were obtained from Fluidigm with the exception of Indium(III)chloride-113 and Indium(III)chloride-115 (Trace Sciences) and Cisplatin-195 and -196 (BuyIsotope). Items from Trace sciences and BuyIsotype were custom orders. The conjugated antibodies were stored in PBS-based antibody stabilizer (Candor Biosciences, cat. #130050). All antibodies were titrated for optimal staining concentrations with control

murine tissues. Full details of the antibodies used and the metals to which they were conjugated are provided in the following table:

Table 1: List of mass cytometry antibodies used and the metals to which they were conjugated.

Barcode stain					
Label	**Target**	**Clone**	**Manufacturer**	**Titre**	**Concentration (µg/ml)**
113In	CD45	30-F11	Biolegend	100	1
115In	CD45	30-F11	Biolegend	100	1
194Pt	CD45	30-F11	Biolegend	100	1
195Pt	CD45	30-F11	Biolegend	100	1
196Pt	CD45	30-F11	Biolegend	100	1
198Pt	CD45	30-F11	Biolegend	100	1
	FC block	93	Biolegend	10	10
FITC	F4/80	BM8	Biolegend	50	2
PE	CD80	16-10A1	Biolegend	50	2
Surface stain					
Label	**Target**	**Clone**	**Manufacturer**	**Titre**	**Concentration (µg/ml)**
141Pr	Ly6G	1A8	Biolegend	100	1
142Nd	CD11c	N418	Biolegend	100	1
143Nd	CD103	2-E7	Biolegend	100	1
144Nd	anti-FITC	FIT22	Fluidigm	100	
145Nd	CD69	H1.2F3	Biolegend	100	1
147Sm	KLRG1	2F1	eBioscience	100	1
148Nd	CD11b	M1/70	Biolegend	100	1
149Sm	Ly6C	HK1.4	Biolegend	200	0.5
150Nd	CD73	TY/11.8	Biolegend	200	0.5
151Eu	CD25	PC61	BD	200	0.5
152Sm	CD3e	145-2C11	Biolegend	100	1
153Eu	CD39	24DMS1	eBio	100	1
154Sm	OX40	OX-86	eBio	100	1
155Gd	PD-1	RMP1-30	Biolegend	100	1
156Gd	anti-PE	PE001	Fluidigm	100	
160Gd	CD62L	MEL-14	Biolegend	400	0.25
162Dy	TIM3	RMT3-23	Fluidigm	50	
163Dy	CD8a	53-6.7	Biolegend	400	0.25
166Er	ICOS	C398.4A	eBioscience	100	1
169Tm	TCRβ	H57-597	Biolegend	100	1
170Er	Nk1.1	PK136	Biolegend	100	1
171Yb	CD44	IM7	Biolegend	400	0.25
172Yb	CD4	RM4-5	Biolegend	200	0.5
173Yb	CD86	GL-1	Biolegend	100	1
174Yb	Lag3	C9B7W	Fluidigm	50	
175Lu	CD38	90	Fluidigm	200	

176Yb	B220	RA3-6B2	Biolegend	200	0.5
209Bi	MHCII	M5/114.15.2	Fluidigm	100	
Intracellular stain					
Label	**Target**	**Clone**	**Manufacturer**	**Titre**	**Concentration (µg/ml)**
146Nd	Helios	22F6	Biolegend	800	0.125
158Gd	Foxp3	FJK-16s	eBio	100	1
159Tb	RORγt	B2D	Fluidigm	100	
161Dy	T-bet	4B10	Biolegend	100	1
164Dy	CTLA-4	UC10-4B9	eBio	100	1
165Ho	BCL6	K112-91	BD	200	0.5
167Er	Gata-3	16E10A23	Biolegend	200	0.5
168Er	KI67	Ki-67	Fluidigm	100	
*Fluidigm antibodies are provided at an unknown concentration					

Mass cytometry CD45 barcoding

For each tumor sample, 1-1.5x10^6 or fewer cells were labelled with metal-conjugated CD45-specific antibodies. Individual tumor samples were incubated with CD45-113In, CD45-115In, CD45-194Pt, CD45-195Pt, CD45-196Pt, or CD45-198Pt antibodies together with Fc-block reagent, and fluorochrome-labeled antibodies for 30 min in room temperature (RT), and then washed twice in CyFACS buffer (PBS with 0.1% BSA and 2mM EDTA). All details of antibodies used for barcoding are listed in **Table 1**.

Staining of antibodies for mass cytometry

Barcoded cells were pooled together and washed in CyFACS buffer then stained with a metal-conjugated surface stain antibody cocktail for 45 min at RT. Cells were then washed twice in CyFACS buffer, stained for viability with the cisplatin analogue dichloro-(ethylenediamine) palladium(II) (103) in PBS for 5min at RT. Using Foxp3 / Transcription Factor Fixation/Permeabilization Concentrate and Diluent (eBiosciences, cat. #00-5523-00), cells were fixed for 30 min at 4°C and permeabilized using 1X permeabilization buffer. Cells were subsequently stained with a metal-conjugated intracellular antibody cocktail for 45 min at 4°C in 1X permeabilization buffer, and then washed twice in CyFACS buffer and once in

PBS. Cells were then fixed overnight in 1.6% paraformaldehyde solution containing DNA Cell-ID Intercalator-103Rh (Fluidigm, cat. #201103A). All details of antibodies used for staining are listed in **Table 1**.

Mass cytometry data acquisition

Prior to data acquisition, cells were washed once in CyFACS buffer and twice in MilliQ H_2O. Cells were then diluted to 1×10^6 cells/mL in MilliQ H_2O containing 15% EQ Four Element Calibration Beads (Fluidigm, cat. #201078) and filtered. Cells were acquired at a rate of 200 to 300 cells/s using a Helios mass cytometer (Fluidigm). Flow Cytometry Standard files were normalized to EQ bead signal.

Mass cytometry data quantification and statistical analysis

For analysis of mass cytometry results, gating and manual debarcoding was performed using CytoBank software. Live $CD45^+$ live cells from all samples in each analysis were clustered together by Clustering Large Analysis (CLARA) using the Statistical Single-Cell Analysis by Fixed Force- and Landmark-Directed (SCAFFoLD) R package (104). Statistical analysis using the Significance Across Microarrays algorithm was performed within statistical SCAFFoLD. SCAFFoLD maps were then generated with manually gated populations as landmarks. Secondary analysis of gated $CD3^+TCRb^+B220^-CD11b^-NK1.1^-CD4^+/CD8a^+$ cells was performed in the same manner, with the exception that X-shift clusters generated within Vortex software (105) were used as the landmarks to help visualize major subpopulations within the SCAFFoLD map. In all experiments, clustering and map generation were performed on all samples to enable the direct comparison between tumor models. Heatmaps and dendrograms were made by heatmap.2 within the gplots package of R software.

Flow cytometry analysis

Freshly harvested MACS-sorted $CD45^+$ lymphocytes, generated as described in *MACS enrichment of CD45+ lymphocytes*, were plated onto 96-well U-bottom plates in FACS buffer. The cell suspensions were blocked with CD16/CD32 antibody (Tonbo Biosciences, cat. #70-0161-M001). Then, cells were incubated in a cocktail of Live/Dead near-IR stain (Invitrogen, cat. #L10119) and surface antibodies prepared in FACS buffer for 30 minutes. For intracellular staining, cells were permeabilized with the FoxP3 transcription factor staining buffer kit (eBioscience, cat. #00-5523-00) as explained before. Cells were then incubated in a cocktail of intracellular antibodies prepared in 1 × Perm/Wash buffer (eBioscience, cat. 00-8333-56) for 45 minutes, and then washed twice in Perm/Wash buffer prior to data collection. Samples were collected on an LSR Fortessa (BD Biosciences), and compensation and data analysis were carried out with FlowJo vX.0.7 (TreeStar). For t-distributed stochastic neighbor embedding analysis, precompensated and gated data were exported from FlowJo. All surface and intracellular antibodies used in this study are listed in the following table:

Table 2: List of Flow cytometry antibodies used.

Antibodies	**Source**	**Identifier**
CD3e-v500 (500A2)	BD Biosciences	Cat. no.: 560771
CD8a-FITC (53-6.7)	eBioscience	Cat. no.: 11-0081-82
CD4-FITC (RM4-5)	Biolegend	Cat. no.: 100509
CD4-BV711	Biolegend	Cat. no.: 317439
CD4-PERCP.CY5.5	Biolegend	Cat. no.: 100433
CD44- BV421 (IM7)	Biolegend	Cat. no.: 103039
CD62L-PECY7	Biolegend	Cat. no.: 104417
CD62L-BV510 (MEL-14)	Biolegend	Cat. no.: 104441
Foxp3-APC (FJK-16S)	Invitrogen	Cat. no.: 17-5773-82
CTLA4-PE (UC10-4B9)	Biolegend	Cat. no.: 106305
LIVE/DEAD™ Fixable Near-IR Dead Cell Stain Kit	Invitrogen	Cat. no.: L34975
B220-APCef780 (RAB-6B2)	Invitrogen	Cat. no.: 47-0452-82
CD11b-APCef780 (M1/70)	Invitrogen	Cat. no.: 47-0112-82
CD11c-APCef780 (N418)	Invitrogen	Cat. no.: 47-0114-82
CD4-APCef780 (N418)	Invitrogen	Cat. no.: 47-0114-82

Granzyme B-PE (NGZB)	Invitrogen	Cat. no.: 12-8898-82
IFN-γ-APC (XMG1.2)	Biolegend	Cat. no.: 505809
CD62L-BV510 (MEL-14)	Biolegend	Cat. no.: 104433
TGF-β-Bv421 (TW7-16B4)	Biolegend	Cat. no.: 141407
F4/80-FITC (BM8)	Biolegend	Cat. no.: 123107
CD11c-PECy7 (N418)	Biolegend	Cat. no.: 117317
CD11b-APC (M1/70)	Biolegend	Cat. no.: 101211
Ly6G-v450 (1A8)	BD Horizon	Cat. no.: 560603
Ly6C-PE (HK1.4)	Biolegend	Cat. no.: 128007
CD3e-V500 (500A2)	BD Horizon	Cat. no.: 560771
B220-V500 (RA3-6B2)	BD Horizon	Cat. no.: 561226
NK1.1-BV510 (PK136)	Biolegend	Cat. no.: 108737

Cytokine stimulation

MACS-sorted $CD45^+$ lymphocytes from mouse tumors were plated onto 96-well U-bottom plates. A cocktail of Phorbol 12-myristate 13-acetate (50 ng/mL; Sigma, cat. #P1585), Ionomycin (0.5 μg/mL; Sigma, cat. #I3909) and Golgi Stop (1:1000 dilution; BD Biosciences, cat. #554724) was prepared in RPMI containing 10% FBS. The cells were incubated in the cocktail for 2 h at 37 °C, and then processed for FACS staining. All surface and intracellular antibodies used in this study are listed in the previous following table.

RNA-seq analysis

Total RNA was extracted from wild-type (WT) or KO KPC and MC38 cells using RNeasy Mini kit (Qiagen, cat. #74134) according to the manufacturer's instructions. In brief, cultured cells were lysed in RLT buffer from the kit and the lysate was transferred to spin column. The spin column was centrifuged for 30 s for flow through and the spin column was washed twice with washed buffer and RNA was eluted in 50 μl elution buffer.

Preparation of cDNA libraries was performed using a TruSeq stranded mRNA sample prep kit (Illumina, cat. #20020594) according to the manufacturer's instructions. Sequencing was performed on an Illumina HiSeq 2500 platform in the 75-base single-end mode. Illumina

Casava1.8.2 software was used for basecalling. Sequenced reads were mapped to the mouse reference genome sequences (mm10) using TopHat version 2.0.13 in combination with Bowtie2 version 2.2.3 and SAMtools version 0.1.19. The fragments per kilobase of exons per million mapped fragments (FPKMs) was calculated using Cuffnorm version 2.2.1. Analysis of the main functions regarding gene expression changes was performed with Ingenuity Pathway Analysis software (IPA®, QIAGEN, https://www.qiagenbioinformatics.com/products/ingenuity-pathway-analysis/). The data have been deposited in the NCBI Gene Expression Omnibus (GEO) database under GEO accession number GSE159967.

Quantitative reverse transcription polymerase chain reaction (qRT-PCR)

Total RNA was extracted from cells (WT or KO or shRNA-treated or Ido1-overexpressing or Ccl2-overexpressing KPC, and WT or KO or shRNA-treated MC38) using RNeasy Mini kit (Qiagen), according to the manufacturer's instructions as explained before. RNAs (15 ng each) were then reverse-transcribed using the SuperScript VILO Master Mix (Invitrogen, cat. #11756050), and qRT-PCR reactions were performed in triplicate using TaqMan Universal PCR Master Mix and TaqMan gene expression assays (cat. #4331182, Applied Biosystems), and measured using 7300 Real Time PCR System (Applied Biosystems). Delta Ct values, which were the Ct values of *Gapdh* subtracted from the Ct values of each gene, were used for normalization, and relative mRNA levels were calculated by 2^ (-delta delta Ct) method. Primers for the genes analyzed are *Ido1* (Mm00492590-m1), *Ccl2* (Mm00441242-m1) and *Arid5a* (Mm005244544-m1), and the normalizing gene *Gapdh* (Mm99999915-m1). All the primers are purchased from Thermofisher.

RNA interference and transfection.

For stable short hairpin RNA (shRNA)-mediated gene silencing, pLKO.1-puro-based recombinant lentiviruses, either generated by ourselves or purchased from Addgene, were used. In brief, shRNAs were constructed in pLKO.1-puro from the Sigma Mission shRNA library. A control scramble shRNA in pLKO.1-puro (Addgene, cat. #1864) were transfected into 293FT cells, together with the envelope plasmid pMD2.G (Addgene, cat. #12259) and the packaging plasmid psPAX2 (Addgene, cat. #12260), using Lipofectamine LTX (Invitrogen, cat. #15338100) according to the manufacturer's instructions. Forty-eight hours after the transfection, culture supernatants were harvested, filtered through 0.45-μm filters (Advantec), and the resultant lentivirus preparations were then applied onto target cells in the presence of Polybrene (8 μg/mL; Nacalai cat. #12996-81). After 24 hours, 4 μg/mL of puromycin (Nacalai cat. #14861-71) was added to the cell culture for one week to select infected cells. The Sigma Mission shRNA library are as follows:

shIdo1 (SHCLNG-NM_008324; TRCN0000066908, TRCN0000066909, TRCN0000066910, TRCN0000066912, TRCN0000066911)

shCcl2 (SHCLNG-NM_011333; TRCN0000301702, TRCN0000301701, TRCN0000304374, TRCN0000034470, TRCN0000034473)

shStat1 (SHCLNGNM_009283; TRCN0000054923, TRCN0000054925, TRCN0000054927, TRCN0000054926, TRCN0000054924)

shARID5A (SHCLNGNM_212481; TRCN0000257353, TRCN0000233529, TRCN0000233530, TRCN0000233531, TRCN0000233532)

Immunoblotting

Cells were lysed on ice with RIPA buffer (1% Nonidet P-40, 150 mM NaCl, 20 mM Tris−HCl, pH 7.4, 5 mM EDTA, 1% Na-deoxycholate, 0.1% SDS, 1 mM Na_3VO_4, 10 μM Na_2MoO_4, 5 μg/mL aprotinin, 2 μg/mL leupeptin, 3 μg/mL pepstatin A and 1 mM

phenylmethylsulfonyl fluoride). Protein concentrations were determined using a Dc protein assay kit (Bio-Rad Laboratories, cat. #5000111JA) with Bovine Serum Albumin (BSA) as a standard. Mixture of reagent A and reagent S was prepared (50:1, vol/vol) from the kit and 20 ul of the mixture is transferred to each well of the 90 well microplate. 5 µl of lysed samples was added to each well and after 15 min of incubation, absorbance was measured at 750 nm using microplate reader. After quantification of protein concentration, all samples were normalized to 2 µg/µl.

Protein samples (20 µg each) were separated by SDS-PAGE and transferred to a polyvinylidene difluoride membrane (Millipore). Membranes were then incubated with the primary antibodies, followed by horseradish peroxidase–conjugated anti–mouse IgG (GE Healthcare, cat. #NA931V). Specific binding was detected using Chemi-Lumi One Ultra, according to the manufacturer's instructions (Nacalai, cat. #11644). Data are shown as representative results of at least two independent experiments. Antibodies used for the experiments are as follows:

Table 3: List of antibodies used for immunoblotting.

Antibodies	**Source**	**Identifier**
Mouse monoclonal IgG anti-ARID5A (P18112)	Invitrogen	Cat. no.: MA5-18292
Mouse Anti-IDO Antibody (10.1)	Millipore	Cat. no.: 05-840
Rabbit monoclonal IgG anti-β-Actin (D6A8) (HRP Conjugate)	CST	Cat. no.: 12620
Rabbit polyclonal IgG anti-STAT1	CST	Cat. no.: 9172
Rabbit monoclonal IgG anti-phospho-Stat1 (Tyr701) (clone 58D6)	CST	Cat. no.: 9167
Rabbit polyclonal IgG anti-Zeb1 antibody	Novus	Cat. no.: NBP105987
Rabbit E-Cadherin (24E10)	CST	Cat. no.: 3195
Mouse monoclonal IgG anti-Flag (M2)	Sigma	Cat. no.: F3165
Mouse monoclonal IgG anti-HA (TANA2)	MBL	Cat. no.: M180-3

ELISA

WT and KO KPC cells were untreated or treated with IFN-γ (2.5 ng/mL; R&D system, cat. #485-MI) and the supernatants were collected at 0, 24, 48, and 72 hours after stimulation. The concentration of Kyn in cell supernatants was measured by the Kyn ELISA kit (ImmuSmol, #BA E-2200), according to the manufacturer's instructions.

WT and KO KPC or MC38 cell supernatants were collected at day 2 and the concentration of Ccl2 was measured using the Mouse CCL2/JE/MCP-1 immunoassy kit (R&D system, cat. #MJEOOB), according to the manufacturer's instructions.

Liquid chromatography coupled with tandem mass spectrometry (LC-MS/MS)

Serum and tumor samples were collected at 10 and 21 days after the implantation of tumors, respectively. The collected samples were immediately frozen in liquid nitrogen and stored in a freezer until analysis. Tumors were homogenized in 4-fold (v/w) of saline, and serum samples were added to acetonitrile containing 1 μg/mL internal standard (Tryptophan-d5 (cat. #DLM-1092-0.5, Kynurenine-d6 (cat. #CLM-9884-PK), and Kynurenic acid-d5 (cat. #DLM-7374-0.01), purchased from Cambridge Isotope Laboratories Inc.), and centrifuged at 13,000 rpm for 5 min at 4°C. Supernatants were injected into the LC-MS/MS system for analysis. The NexeraX2 liquid chromatography system (Shimadzu, Kyoto, Japan) with QTRAP 4500 mass-spectrometer (AB SCIEX, Framingham, MA, USA) equipped with an electrospray ionization (ESI) source was used for the quantification of Trp, Kyn, and kynurenic acid. The analytes were separated on an Intrada amino acid column (2.1 mm × 50 mm; 3.0 μm particle size; Imtakt, Kyoto, Japan), with the column temperature set at 40ºC. The mobile phase consisting of an aqueous phase (A: 100 mM ammonium formate in water) and an organic phase (B: 0.1% formic acid in acetonitrile) was used for a gradient elution at a flow rate of 0.5 mL/min. The HPLC elution program was as follows: 80% B (0.5 min) → 0% B (linear

decrease in 1.5 min) → 80% B (linear increase in 0.5 min) → 80% B (0.5 min). Multiple reaction monitoring was performed using individually optimized conditions.

Table 4: MRM transition parameters of analytes and internal standards.

Analyte	**MRM transition (*m/z*)**	**DP* (V)**	**CE* (eV)**	**CXP* (V)**
L-Tryptophan	205.0 > 187.9	43	15	12
L-Kynurenine	209.0 > 191.9	51	11	14
Kynurenic acid	190.0 > 144.0	41	27	36
L-Tryptophan-d5	210.0 > 192.9	43	15	12
L-Kynurenine-d6	215.1 > 197.9	40	13	18
Kynurenic acid-d5	195.0 > 149.0	41	27	36
*DP: declustering potential, CE: collision energy, CXP: collision cell exit potential				

RNA stability assay

WT or KO KPC cells were stimulated with IFN-γ (5 ng/mL) for 6 hours, which is shown as the zero-time point. Cells were then treated with actinomycin D (2 μg/mL; Sigma, #A9415), and total RNA was harvested at the indicated times using RNeasy Mini kit. *Ido1* transcripts were quantified by qRT-PCR analysis, and the amount of the *Ido1* transcripts at 0 min were normalized to 100%. The percentage of mRNA remaining at serial time points compared with the 0 min time point were plotted and the half-lives of cytokine mRNAs were determined by nonlinear regression curve fitting (one-phase decay) using GraphPad software.

Luciferase reporter gene assay

To generate the luciferase plasmid constructs, DNA fragments of the 3′-UTRs of *Ido1* and *Ccl2* mRNAs were prepared with the PCR amplification using cDNAs of KPC cells, as a template. The PCR cycling conditions were 98 °C for 2 min, followed by 30 cycles of 98 °C

for 10s, 60 °C for 30s and 68 °C for 3 min, and single cycle of 68 °C for 10s. The PCR products were subcloned into the pmirNanoGlo luciferase plasmid (Promega, cat. #CS194105) using the In-Fusion HD kit (Takara, cat. #Z9649N) according to the manufacturer's instructions. Arid5a-deficient KPC cells cultured in 24-well plates were transfected with either the pmirNanoGlo luciferase plasmid encoding the 3′-UTR region, or the pmirNanoGlo luciferase control plasmid (50 ng). All transfections were performed in combination with Arid5a pcDNA3-Flag (600 ng) or the empty pcDNA3-Flag vector (600 ng). The pmirNanoGlo luciferase control plasmid was used as a negative control, and the empty vector was used to equalize the total amount of DNA. Transfections were performed using the Lipofectamine 3000 kit (ThermoFisher, cat. #L3000015). After 8 hours, cells were lysed using passive lysis buffer. Luciferase activity was measured using the Nano-Glo® Dual-Luciferase® Reporter Assay System (Promega, cat. #N1630). Firefly luciferase activity was normalized by Renella luciferase activity, and expressed as the fold stimulation relative to the activity in vector-transfected cells. The primers used for amplifying the cDNAs for cloning are as follows:

Ido1 3'-UTR (Forward) 5'-agcctcgagtctagatgtagcaagctccacttctat-3'

Ido1 3'-UTR (Reverse) 5'-gctcgaagcggccgctcaacttcacaataactttta-3'

Ccl2 3'-UTR (Forward) 5'-agcctcgagtctagatgtgactcggactgtgatgc-3'

Ccl2 3'-UTR (Reverse) 5'-gctcgaagcggccgctggtgtacaaaaataatatatt-3'

Ido1 CDS (Forward) 5'-ctagactgccggatccatggcgtatgtgtggaaccga-3'

Ido1 CDS (Reverse) 5'-aattgttaccgcggccgcctaaggccaactcagaagagc-3'

Ccl2 CDS (Forward) 5'-ctagactgccggatccgcaggtccctgtcatgcttctg-3'

Ccl2 CDS (Reverse) 5'-aattgttaccgcggccgcctagttcactgtcacactggtc-3'

Arid5a CDS (Forward) 5'-ttacgctagcgaattcatggcagcacctccggccaaagggaacaca-3'

Arid5a CDS (Reverse) 5'-attgttaccgcggccgcctacagtttggtgttgaggtggaagaag-3'

Arid5a-ΔM CDS (Forward) 5’-tagactgccggatccatggactacaaggacgacga-3’

Arid5a-ΔM CDS (Reverse) 5’-aattgttaccgcggccgcttactactacagtttggtgt-3’

RNA pulldown assay

The RNA binding assay was performed using RiboTrap Kit (MBL, cat. #RN1011) according to the manufacturer’s instructions. Briefly, the 3′ -UTRs of *Ido1* and *Ccl2* mRNA were amplified by PCR and subcloned into the pBluescript SK(-) plasmid, from Dr. Sabe (Hokkaido University), using the In-Fusion HD kit. To modify these RNAs, uing Riboprobe® Systems (Promega, cat. #P1440), 5-bromo-UTP (BrU) included in the RiboTrap Kit, was randomly incorporated into the 3′-UTR of *Ido1* or *Ccl2* upon *in vitro* transcription. The quality and concentration of BrU-labeled RNAs were assessed using the Bioanalyzer 2100 (Agilent) with the RNA 6000 Nano Kit (Agilent, cat. #5067-1511). Anti-BrU antibody were conjugated to Invitrogen Dynabeads (Invitrogen, cat. #10004D) for overnight at 4°C, and were washed with wash buffer provided in RiboTrap Kit. Anti-BrU conjugated beads were then incubated for 3 hrs. at 4°C with the BrU-labeled RNAs. Then, recombinant Arid5a protein was transferred to the mixture followed by 2 hrs. of incubation at 4°C. The samples were then washed and eluted, and were subjected to SDS-PAGE. Primers used for this study are as follows:

Ido1 3’-UTR (Forward) 5’-agcctcgagtctagatgtagcaagctccacttctat-3’

Ido1 3’-UTR (Reverse) 5’-gctcgaagcggccgctcaacttcacaataactttta-3’

Ccl2 3’-UTR (Forward) 5’-agcctcgagtctagatgtgactcggactgtgatgc-3’

Ccl2 3’-UTR (Reverse) 5’-gctcgaagcggccgctggtgtacaaaaataatatatt-3’

Genomic data analysis

Normalized RNA-seq expression data for pancreatic cancer (Study ID: QCMG) were downloaded from cBioPortal, an open platform for cancer genomics data (23,24). Then, 96 samples tagged as ICGC were extracted for the subtype analysis mentioned in the paper (25). As for colorectal cancer, data were obtained via Synapse (ID: syn2623706) mentioned in the paper (26) and 512 samples tagged as TCGA were analyzed. Dunn's multiple comparisons test was used for the comparison of mRNA expression levels among the cancer subtypes.

For Spearman's correlation analysis between *ARID5A* and other genes, datasets of TCGA PanCancer Atlas (168 and 592 samples for pancreas and colon cancer respectively) were used and their analyses were conducted on the cBioPortal site (https://www.cbioportal.org/).

Immunofluorescence microscopy

Immunofluorescence microscopy analysis was performed according to the method described previously(101). Briefly, WT KPC cells were incubated with or without TGFβ (5 ng/mL; R&D system, cat. #240-B) for 48 hours before fixation with 4% paraformaldehyde in PBS (with no detergent). Cells were then subjected to immunostaining using an anti-E-cadherin antibody (CST, cat. #3195), followed by an Alexa Fluor 488-conjugated secondary antibody (Molecular Probes, cat. #A11006). F-actin was visualized using Texas Red-X-conjugated phalloidin (Molecular Probes, cat. #T7471), and nuclei were stained with DAPI before mounting with 50% glycerol in PBS. Fluorescence images were obtained using a confocal laser-scanning microscope (Model A1R with NIS-Elements, Nikon) using a CFI Plan Apo VC 60 × H oil-immersion objective with an NA of 1.4, and analyzed using the attached software. Data were collected from two independent experiments, each analyzing at least 10 cells. Images were handled using Photoshop version 7 (Adobe).

Statistical analysis

Statistical significance was calculated between two groups by the unpaired student *t*-test. One-way Analysis of variance (ANOVA) followed by the Tukey's Honestly Significant Difference post-test was used to calculate statistical significance between multiple groups. Statistical significance of the survival data was calculated by Kaplan-Meier with long-rank analysis. Analyses were performed using GraphPad Prism 8. Error bars represent the standard error of mean (SEM) and a *p*-value of less than 0.05 was considered to indicate a statistically significant difference between groups. Figure legends specify the test used, criteria for statistical significance, and the number of experimental, biological, and technical replicates.

References

1. B. M. Gumbiner, Epithelial morphogenesis. *Cell* **69**, 385–387 (1992).
2. R. Kalluri, E. G. Neilson, Epithelial-mesenchymal transition and its implications for fibrosis. *J. Clin. Invest.* **112**, 1776–1784 (2003).
3. J. P. Their, Epithelial-mesenchymal transitions in tumor progression. *Nat. Rev. Cancer* **2**, 442–454 (2002).
4. M. A. Nieto, R. Y. Y. J. Huang, R. A. A. Jackson, J. P. P. Thiery, EMT: 2016. *Cell* **166**, 21–45 (2016).
5. C. Yeaman, K. K. Grindstaff, M. D. H. Hansen, W. J. Nelson, Cell polarity: Versatile scaffolds keep things in place. *Curr. Biol.* **9**, R515–R517 (1999).
6. M. P. Stemmler, R. L. Eccles, S. Brabletz, T. Brabletz, Non-redundant functions of EMT transcription factors. *Nat. Cell Biol.* **21**, 102–112 (2019).
7. J. Yang, *et al.*, Guidelines and definitions for research on epithelial–mesenchymal transition. *Nat. Rev. Mol. Cell Biol.* **21**, 341–352 (2020).
8. A. M. Krebs, *et al.*, The EMT-activator Zeb1 is a key factor for cell plasticity and promotes metastasis in pancreatic cancer. *Nat. Cell Biol.* **19**, 518–529 (2017).
9. T. Shibue, R. A. Weinberg, EMT, CSCs, and drug resistance: The mechanistic link and clinical implications. *Nat. Rev. Clin. Oncol.* **14**, 611–629 (2017).
10. I. Pastushenko, *et al.*, Identification of the tumour transition states occurring during EMT. *Nature* **556**, 463–468 (2018).
11. E. Romeo, C. A. Caserta, C. Rumio, F. Marcucci, The Vicious Cross-Talk between Tumor Cells with an EMT Phenotype and Cells of the Immune System. *Cells* **8**, 460 (2019).
12. W. Lu, Y. Kang, Epithelial-Mesenchymal Plasticity in Cancer Progression and Metastasis. *Dev. Cell* **49**, 361–374 (2019).

13. P. B. Gupta, I. Pastushenko, A. Skibinski, C. Blanpain, C. Kuperwasser, Phenotypic Plasticity: Driver of Cancer Initiation, Progression, and Therapy Resistance. *Cell Stem Cell* **24**, 65–78 (2019).

14. M. Binnewies, *et al.*, Understanding the tumor immune microenvironment (TIME) for effective therapy. *Nat. Med.* **24**, 541–550 (2018).

15. T. L. Whiteside, The tumor microenvironment and its role in promoting tumor growth. *Oncogene* **27**, 5904–5912 (2008).

16. Y. K. Chae, *et al.*, Epithelial-mesenchymal transition (EMT) signature is inversely associated with T-cell infiltration in non-small cell lung cancer (NSCLC). *Sci. Rep.* **8**, 1–8 (2018).

17. N. M. Aiello, *et al.*, EMT Subtype Influences Epithelial Plasticity and Mode of Cell Migration Developmental Cell Article EMT Subtype Influences Epithelial Plasticity and Mode of Cell Migration. *Dev. Cell* **45**, 681–695 (2018).

18. R. Kalluri, The biology and function of fibroblasts in cancer. *Nat. Rev. Cancer* **16**, 582–598 (2016).

19. A. W. Lambert, D. R. Pattabiraman, R. A. Weinberg, Emerging Biological Principles of Metastasis. *Cell* **168**, 670–691 (2017).

20. P. Sharma, J. P. Allison, The future of immune checkpoint therapy. *Science (80-.).* **348**, 56–61 (2015).

21. V. Koliaraki, A. Prados, M. Armaka, G. Kollias, The mesenchymal context in inflammation, immunity and cancer. *Nat. Immunol.* **21**, 974–982 (2020).

22. J. Galon, D. Bruni, Approaches to treat immune hot, altered and cold tumours with combination immunotherapies. *Nat. Rev. Drug Discov.* **18**, 197–218 (2019).

23. N. Nagarsheth, M. S. Wicha, W. Zou, Chemokines in the cancer microenvironment and their relevance in cancer immunotherapy. *Nat. Rev. Immunol.* **17**, 559–572 (2017).

24. R. H. Vonderheide, The Immune Revolution: A Case for Priming, Not Checkpoint. *Cancer Cell* **33**, 563–569 (2018).

25. C. Grasselly, *et al.*, The antitumor activity of combinations of cytotoxic chemotherapy and immune checkpoint inhibitors is model-dependent. *Front. Immunol.* **9**, 1–13 (2018).

26. S. I. S. Mosely, *et al.*, Rational selection of syngeneic preclinical tumor models for immunotherapeutic drug discovery. *Cancer Immunol. Res.* **5**, 29–41 (2017).

27. A. Amedei, E. Niccolai, D. Prisco, Human Vaccines & Immunotherapeutics Pancreatic cancer: Role of the immune system in cancer progression and vaccine-based immunotherapy Pancreatic cancer: Role of the immune system in cancer progression and vaccine-based immunotherapy. **10**, 3354–3368 (2014).

28. L. L. van der Woude, M. A. J. Gorris, A. Halilovic, C. G. Figdor, I. J. M. de Vries, Migrating into the Tumor: a Roadmap for T Cells. *Trends in Cancer* **3**, 797–808 (2017).

29. W. Zheng, *et al.*, Combination of radiotherapy and vaccination overcome checkpoint blockade resistance. *Oncotarget* **7**, 43039–43051 (2016).

30. J. Galon, D. Bruni, Tumor Immunology and Tumor Evolution: Intertwined Histories. *Immunity* **52**, 55–81 (2020).

31. C. E. Clark, *et al.*, Dynamics of the immune reaction to pancreatic cancer from inception to invasion. *Cancer Res.* **67**, 9518–9527 (2007).

32. D. I. Gabrilovich, S. Ostrand-Rosenberg, V. Bronte, Coordinated regulation of myeloid cells by tumours. *Nat. Rev. Immunol.* **12**, 253–268 (2012).

33. J. Roelands, *et al.*, Immunogenomic classification of colorectal cancer and therapeutic implications. *Int. J. Mol. Sci.* **18**, 2229 (2017).

34. A. B. Blair, *et al.*, IDO1 inhibition potentiates vaccine-induced immunity against

pancreatic adenocarcinoma. *J. Clin. Invest.* **129**, 1742–1755 (2019).

35. P. Sharma, S. Hu-Lieskovan, J. A. Wargo, A. Ribas, Primary, Adaptive, and Acquired Resistance to Cancer Immunotherapy. *Cell* **168**, 707–723 (2017).

36. X. Xu, L. Ye, K. Araki, R. Ahmed, MTOR, linking metabolism and immunity. *Semin. Immunol.* **24**, 429–435 (2012).

37. R. J. Deberardinis, N. S. Chandel, Fundamentals of cancer metabolism INTRODUCTION AND OVERARCHING PRINCIPLES. *Sci. Adv.* **2**, 1–18 (2016).

38. E. Menares, *et al.*, Tissue-resident memory CD8+ T cells amplify anti-tumor immunity by triggering antigen spreading through dendritic cells. *Nat. Commun.* **10**, 4401 (2019).

39. J. D. Mezrich, *et al.*, An Interaction between Kynurenine and the Aryl Hydrocarbon Receptor Can Generate Regulatory T Cells. *J. Immunol.* **185**, 3190–3198 (2010).

40. D. H. Munn, A. L. Mellor, IDO in the Tumor Microenvironment: Inflammation, Counter-Regulation, and Tolerance. **37**, 193–207 (2016).

41. A. L. Mellor, D. H. Munn, Tryptophan Catabolism and Regulation of Adaptive Immunity. *J. Immunol.* **170**, 5809–5813 (2003).

42. J. E. Cheong, L. Sun, Targeting the IDO1/TDO2–KYN–AhR Pathway for Cancer Immunotherapy – Challenges and Opportunities. *Trends Pharmacol. Sci.* **39**, 307–325 (2018).

43. J. Godin-Ethier, L. A. Hanafi, C. A. Piccirillo, R. Lapointe, Indoleamine 2,3-dioxygenase expression in human cancers: Clinical and immunologic perspectives. *Clin. Cancer Res.* **17**, 6985–6991 (2011).

44. M. Liu, *et al.*, Targeting the IDO1 pathway in cancer: From bench to bedside. *J. Hematol. Oncol.* **11**, 1–12 (2018).

45. O. Takikawa, A. Habara-Ohkubo, R. Yoshida, IFN-gamma is the inducer of indoleamine 2,3-dioxygenase in allografted tumor cells undergoing rejection. *J.*

Immunol. **145**, 1246–1250 (1990).

46. W.-P. M. Urquhart, *et al.*, RNA Interference Immunosuppressive Molecule IDO through Inhibiting Tumor-Derived Reinstalling Antitumor Immunity by. *J. Immunol.* **177**, 5639–5646 (2006).

47. L. Zhai, *et al.*, IDO1 in cancer: a Gemini of immune checkpoints. *Cell. Mol. Immunol.* **15**, 447–457 (2018).

48. C. Uyttenhove, *et al.*, Evidence for a tumoral immune resistance mechanism based on tryptophan degradation by indoleamine 2,3-dioxygenase. *Nat. Med.* **9**, 1269–1274 (2003).

49. S. L. Deshmane, S. Kremlev, S. Amini, B. E. Sawaya, Monocyte chemoattractant protein-1 (MCP-1): An overview. *J. Interf. Cytokine Res.* **29**, 313–325 (2009).

50. M. C. Miller, K. H. Mayo, Molecular Sciences Chemokines from a Structural Perspective. *Int. J. Mol. Sci.* **18**, 2088 (2017).

51. T. Yoshimura, The chemokine MCP-1 (CCL2) in the host interaction with cancer: A foe or ally? *Cell. Mol. Immunol.* **15**, 335–345 (2018).

52. B. H. Li, M. A. Garstka, Z. F. Li, Chemokines and their receptors promoting the recruitment of myeloid-derived suppressor cells into the tumor. *Mol. Immunol.* **117**, 201–215 (2020).

53. D. Wilsker, *et al.*, Nomenclature of the ARID family of DNA-binding proteins. *Genomics* **86**, 242–251 (2005).

54. B. Zheng, H. He, Y. Zheng, W. Wu, S. McCormick, An ARID Domain-Containing Protein within Nuclear Bodies Is Required for Sperm Cell Formation in Arabidopsis thaliana. *PLoS Genet.* **10**, 1004421 (2014).

55. J. Iwahara, R. T. Clubb, Solution structure of the DNA binding domain from Dead ringer, a sequence-specific AT-rich interaction domain (ARID). *EMBO J.* **18**, 6084–

6094 (1999).

56. R. D. Kortschak, P. W. Tucker, R. Saint, ARID proteins come in from the desert. *Trends Biochem. Sci.* **25**, 294–299 (2000).

57. S. Kang, T. Tanaka, M. Narazaki, T. Kishimoto, Targeting Interleukin-6 Signaling in Clinic. *Immunity* **50**, 1007–1023 (2019).

58. K. Masuda, *et al.*, Arid5a controls IL-6 mRNA stability, which contributes to elevation of IL-6 level in vivo. *Proc Natl Acad Sci U S A* **110**, 9409–9414 (2013).

59. J. P. Chalise, *et al.*, Feedback regulation of Arid5a and Ppar-γ2 maintains adipose tissue homeostasis. *Proc. Natl. Acad. Sci. U. S. A.* **116**, 15128–15133 (2019).

60. K. K. Nyati, R. G. Agarwal, P. Sharma, T. Kishimoto, Arid5a Regulation and the Roles of Arid5a in the Inflammatory Response and Disease. *Front. Immunol.* **10**, 2790 (2019).

61. T. Tanaka, M. Narazaki, T. Kishimoto, IL-6 in inflammation, immunity, and disease. *Cold Spring Harb. Perspect. Biol.* **6**, a016295 (2014).

62. Y. Lou, *et al.*, Epithelial-mesenchymal transition is associated with a distinct tumor microenvironment including elevation of inflammatory signals and multiple immune checkpoints in lung adenocarcinoma. *Clin. Cancer Res.* **22**, 3630–3642 (2016).

63. A. Dongre, R. A. Weinberg, New insights into the mechanisms of epithelial–mesenchymal transition and implications for cancer. *Nat. Rev. Mol. Cell Biol.* **20**, 69–84 (2019).

64. X. Zheng, *et al.*, Epithelial-to-mesenchymal transition is dispensable for metastasis but induces chemoresistance in pancreatic cancer. *Nature* **527**, 525–530 (2015).

65. R. L. Porter, *et al.*, Epithelial to mesenchymal plasticity and differential response to therapies in pancreatic ductal adenocarcinoma. *Proc. Natl. Acad. Sci. U. S. A.* **116**, 26835–26845 (2019).

66. P. Bailey, *et al.*, Genomic analyses identify molecular subtypes of pancreatic cancer. *Nature* **531**, 47–52 (2016).

67. M. B. Wachsmann, L. M. Pop, E. S. Vitetta, Pancreatic ductal adenocarcinoma: a review of immunologic aspects. *J. Investig. Med.* **60**, 643–63 (2012).

68. E. P. Kopantzev, *et al.*, Activation of IGF/IGF-IR signaling pathway fails to induce epithelial-mesenchymal transition in pancreatic cancer cells. *Pancreatology* **19**, 390–396 (2019).

69. A. V. Biankin, *et al.*, Pancreatic cancer genomes reveal aberrations in axon guidance pathway genes. *Nature* **491**, 399–405 (2012).

70. R. H. Hruban, *et al.*, An Illustrated Consensus on the Classification of Pancreatic Intraepithelial Neoplasia and Intraductal Papillary Mucinous Neoplasms. *Am. J. Surg. Pathol.* **28**, 977–987 (2004).

71. N. Waddell, *et al.*, Whole genomes redefine the mutational landscape of pancreatic cancer. *Nature* **518**, 495–501 (2015).

72. S. R. Hingorani, *et al.*, Trp53R172H and KrasG12D cooperate to promote chromosomal instability and widely metastatic pancreatic ductal adenocarcinoma in mice. *Cancer Cell* **7**, 469–483 (2005).

73. M. K. Wendt, T. M. Allington, W. P. Schiemann, Mechanisms of the epithelial-mesenchymal transition by TGF-β. *Futur. Oncol.* **5**, 1145–1168 (2009).

74. J. Xu, S. Lamouille, R. Derynck, TGF-B-induced epithelial to mesenchymal transition. *Cell Res.* **19**, 156–172 (2009).

75. C. J. David, J. Massagué, Contextual determinants of TGFβ action in development, immunity and cancer. *Nat. Rev. Mol. Cell Biol.* **19**, 419–435 (2018).

76. D. E. Johnson, R. A. O'Keefe, J. R. Grandis, Targeting the IL-6/JAK/STAT3 signalling axis in cancer. *Nat. Rev. Clin. Oncol.* **15**, 234–248 (2018).

77. T. F. Gajewski, H. Schreiber, Y.-X. Fu, Innate and adaptive immune cells in the tumor microenvironment. *Nat. Immunol.* **14**, 1014–1022 (2013).

78. C. V. Ramana, M. P. Gil, R. D. Schreiber, G. R. Stark, Stat1-dependent and -independent pathways in IFN-γ-dependent signaling. *Trends Immunol.* **23**, 96–101 (2002).

79. D. E. Sanford, *et al.*, Inflammatory monocyte mobilization decreases patient survival in pancreatic cancer: A role for targeting the CCL2/CCR2 axis. *Clin. Cancer Res.* **19**, 3404–3415 (2013).

80. J. Guinney, *et al.*, The consensus molecular subtypes of colorectal cancer. *Nat. Med.* **21**, 1350–1356 (2015).

81. A. E. Yuzhalin, *et al.*, Proteomics analysis of the matrisome from MC38 experimental mouse liver metastases. *Am. J. Physiol. - Gastrointest. Liver Physiol.* **317**, G625-E639 (2019).

82. B. Zhang, *et al.*, Antimetastatic Role of Smad4 Signaling in Colorectal Cancer. *Gastroenterology* **138**, 969–980 (2010).

83. S. Mariathasan, *et al.*, TGFβ attenuates tumour response to PD-L1 blockade by contributing to exclusion of T cells. *Nature* **554**, 544–548 (2018).

84. J. Zhu, H. Yamane, W. E. Paul, Differentiation of effector CD4+ T cell populations. *Annu. Rev. Immunol.* **28**, 445–489 (2010).

85. E. J. Wherry, *et al.*, Lineage relationship and protective immunity of memory CD8T cell subsets. *Nat. Immunol.* **4**, 225–234 (2003).

86. T. Phan, *et al.*, Salmonella-mediated therapy targeting indoleamine 2, 3-dioxygenase 1 (IDO) activates innate immunity and mitigates colorectal cancer growth. *Cancer Gene Ther.* **27**, 235–245 (2020).

87. J. Li, *et al.*, Tumor Cell-Intrinsic Factors Underlie Heterogeneity of Immune Cell

Infiltration and Response to Immunotherapy. *Immunity* **49**, 178–193 (2018).

88. D. S. Chen, I. Mellman, Oncology meets immunology: The cancer-immunity cycle. *Immunity* **39**, 1–10 (2013).

89. P. S. Hegde, D. S. Chen, Perspective Top 10 Challenges in Cancer Immunotherapy. *Immunity* **52**, 17–35 (2020).

90. S. Lamouille, J. Xu, R. Derynck, Molecular mechanisms of epithelial–mesenchymal transition. *Nat. Rev. Mol. Cell Biol.* **15**, 178–196 (2014).

91. N. J. Sullivan, *et al.*, Interleukin-6 induces an epithelial–mesenchymal transition phenotype in human breast cancer cells. *Oncogene* **28**, 2940–2947 (2009).

92. A. Yadav, B. Kumar, J. Datta, T. N. Teknos, P. Kumar, IL-6 promotes head and neck tumor metastasis by inducing epithelial-mesenchymal transition via the JAK-STAT3-SNAIL signaling pathway. *Mol. Cancer Res.* **9**, 1658–1667 (2011).

93. D. Bruni, H. K. Angell, J. Galon, The immune contexture and Immunoscore in cancer prognosis and therapeutic efficacy. *Nat. Rev. Cancer* **20**, 662–680 (2020).

94. A. J. Muller, M. G. Manfredi, Y. Zakharia, G. C. Prendergast, Inhibiting IDO pathways to treat cancer: lessons from the ECHO-301 trial and beyond. *Semin. Immunopathol.* **41**, 41–48 (2019).

95. T. C. Mitchell, *et al.*, Epacadostat plus pembrolizumab in patients with advanced solid tumors: Phase I results from a multicenter, open-label phase I/II trial (ECHO-202/KEYNOTE-037). *J. Clin. Oncol.* **36**, 3223–3230 (2018).

96. T. M. Nywening, *et al.*, Targeting tumour-associated macrophages with CCR2 inhibition in combination with FOLFIRINOX in patients with borderline resectable and locally advanced pancreatic cancer: A single-centre, open-label, dose-finding, non-randomised, phase 1b trial. *Lancet Oncol.* **17**, 651–662 (2016).

97. A. Kalbasi, *et al.*, Tumor-derived CCL2 mediates resistance to radiotherapy in

pancreatic ductal adenocarcinoma. *Clin. Cancer Res.* **23**, 137–148 (2017).

98. W. Bin Fang, *et al.*, CCL2/CCR2 chemokine signaling coordinates survival and motility of breast cancer cells through Smad3 protein- and p42/44 mitogen-activated protein kinase (MAPK)-dependent mechanisms. *J. Biol. Chem.* **287**, 36593–36608 (2012).

99. J. Galon, W. H. Fridman, F. Pages, The adaptive immunologic microenvironment in colorectal cancer: A novel perspective. *Cancer Res.* **67**, 1883–1886 (2007).

100. S. R. Hingorani, *et al.*, Preinvasive and invasive ductal pancreatic cancer and its early detection in the mouse. *Cancer Cell* **4**, 437–450 (2003).

101. S. Hashimoto, *et al.*, ARF6 and AMAP1 are major targets of KRAS and TP53 mutations to promote invasion, PD-L1 dynamics, and immune evasion of pancreatic cancer. *Proc. Natl. Acad. Sci. U. S. A.* **116**, 17450–17459 (2019).

102. H. E. Mei, M. D. Leipold, H. T. Maecker, Platinum-conjugated antibodies for application in mass cytometry. *Cytom. Part A* **89**, 292–300 (2016).

103. F. J. Hartmann, E. F. Simonds, S. C. Bendall, A Universal Live Cell Barcoding-Platform for Multiplexed Human Single Cell Analysis. *Sci. Rep.* **8**, 10770 (2018).

104. M. H. Spitzer, *et al.*, An interactive reference framework for modeling a dynamic immune system. *Science (80-.).* **349**, 1259425–1259425 (2015).

105. N. Samusik, Z. Good, M. H. Spitzer, K. L. Davis, G. P. Nolan, Automated mapping of phenotype space with single-cell data. *Nat. Methods* **13**, 493–496 (2016).

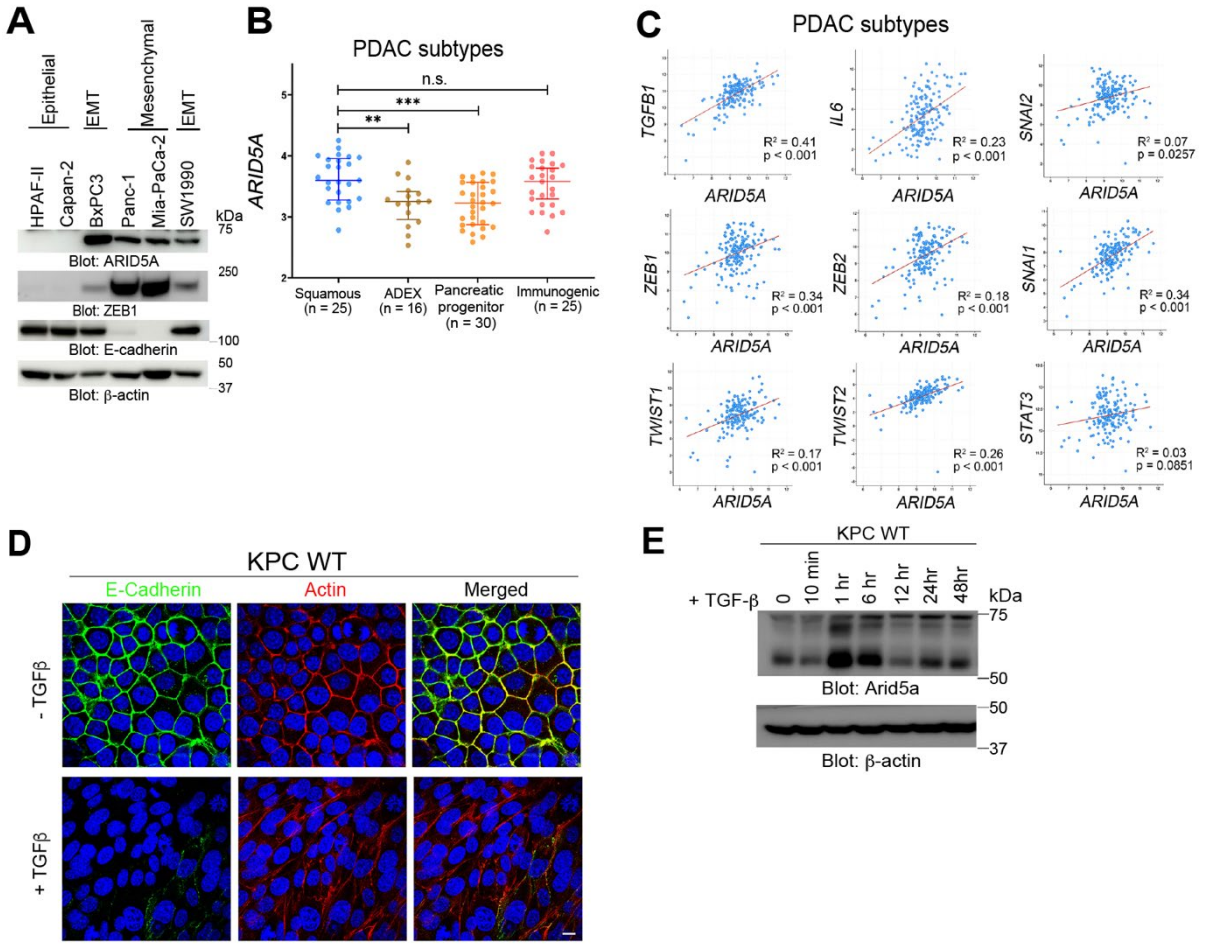

Fig. 1: Arid5a is expressed in mesenchymal tumor subtypes.
A, Immunoblot analysis of indicated proteins in representative human pancreatic cancer cell lines. **B,** *ARID5A* mRNA levels among various PDAC subtypes as analyzed by RNA sequencing. **C,** Statistical correlation of the expression levels of ARID5A and EMT associated genes in the TCGA RNAseq. dataset of human primary pancreatic tumors (n = 165). **D,** Representative images of immunofluorescence staining for E-cadherin (green) and F-actin (red) in WT and KO KPC cells untreated or treated with TGF-β (5 ng/mL). Scale bar, 500 μm. **E,** KPC cells were untreated or treated with TGF-β, and protein expression was analyzed by immunoblotting. n.s., nonsignificant; $^{**}p < 0.01$, $^{***}p < 0.001$; Data are shown as the mean ± SEM, and were analyzed by one way ANOVA. Data are representative of three independent experiments (**A, D,** and **E**).

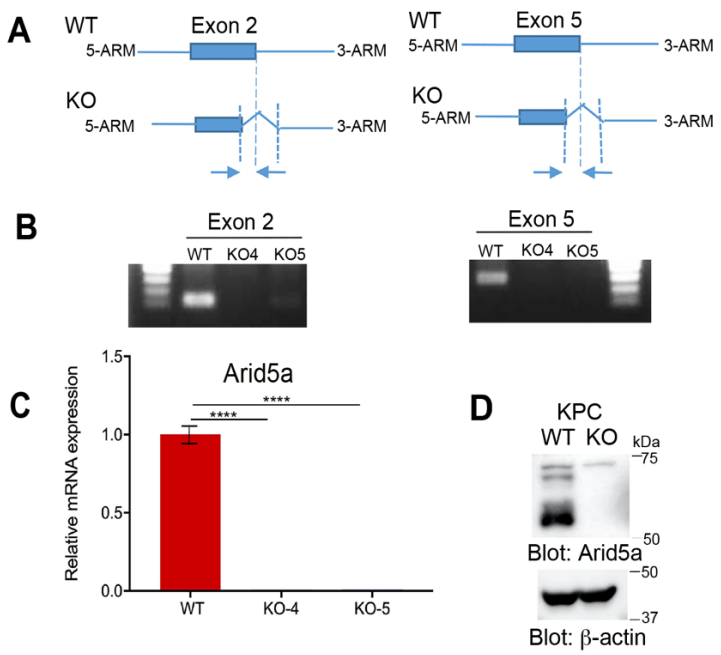

Fig. 2: Generation of Arid5a KO KPC cells using CRISPR-Cas9.
A, Schematic diagram of the deletion region of exon 2 and 5 of *Arid5a*. The diagram shows the regions of the primers used for genomic PCR to determine the deletion in exon 2 and exon 5. **B,** Expression of *Arid5a* indicated exons in KPC cells as analyzed by genomic PCR. **C,** *Arid5a* mRNA expression in WT and KO KPC cells as analyzed by qRT-PCR. **D,** immunoblot analysis of indicated proteins in WT and KO KPC cells. $^{****}p < 0.0001$; Data are shown as the mean ± SEM, and were analyzed by one way ANOVA with post-hoc Tukey's test. Data are representative of three independent experiments (**B, C** and **D**).

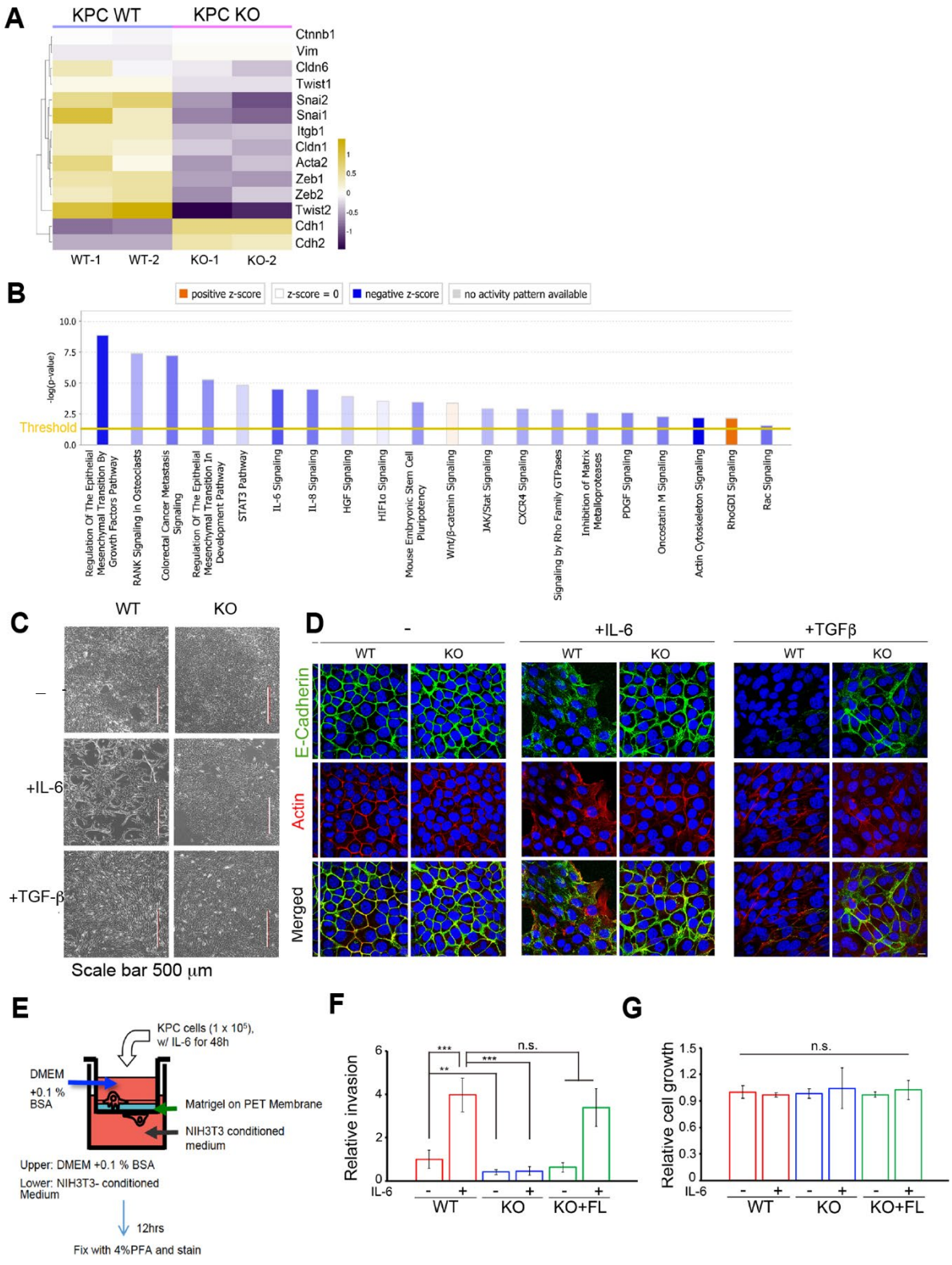

Fig. 3: Arid5a plays crucial roles in IL-6- and TGF-β-induced mesenchymal phenotypes of KPC cells.

A, Heatmap showing differentially expressed genes between WT and KO KPC cells analyzed by RNAseq. **B,** IPA of differentially expressed genes in WT relative to KO KPC cells. Only those genes with a fold change ≥ 2 and a false discovery rate ≤ 0.05 were imported into IPA. A greater color intensity indicates a stronger enrichment of Z-score, both positive (orange)

and negative (blue). The ratio demonstrates the proportion of genes represented in our dataset relative to all known genes in the IPA database for a given pathway. **C,** WT and KO KPC cells were untreated or treated with IL-6 (10 ng/mL) or TGF-β (5 ng/mL) for 48 h and analyzed by confocal microscopy. Scale bar, 500 μm. **D,** Representative images of immunofluorescence staining for E-cadherin (green) and F-actin (red) in WT and KO KPC cells untreated or treated with IL-6 (10 ng/mL) or TGF-β (5 ng/mL) for 48 h. **E,** Schematic view for Matrigel invasion assay. **F,** Relative invasion activity of WT, KO, and Arid5a-expressing KO KPC cells untreated or treated with IL-6 for 48 h was measured by the Matrigel invasion assay. **G,** Relative cell growth of WT, KO, and Arid5a-expressing KO KPC cells. n.s., nonsignificant; $^{**}p < 0.01$, $^{***}p < 0.001$; Data are shown as the mean ± SEM, and were analyzed by one way ANOVA with post-hoc Tukey's test. Data are representative of two (**A**) or three (**C, D, F and G**) independent experiments.

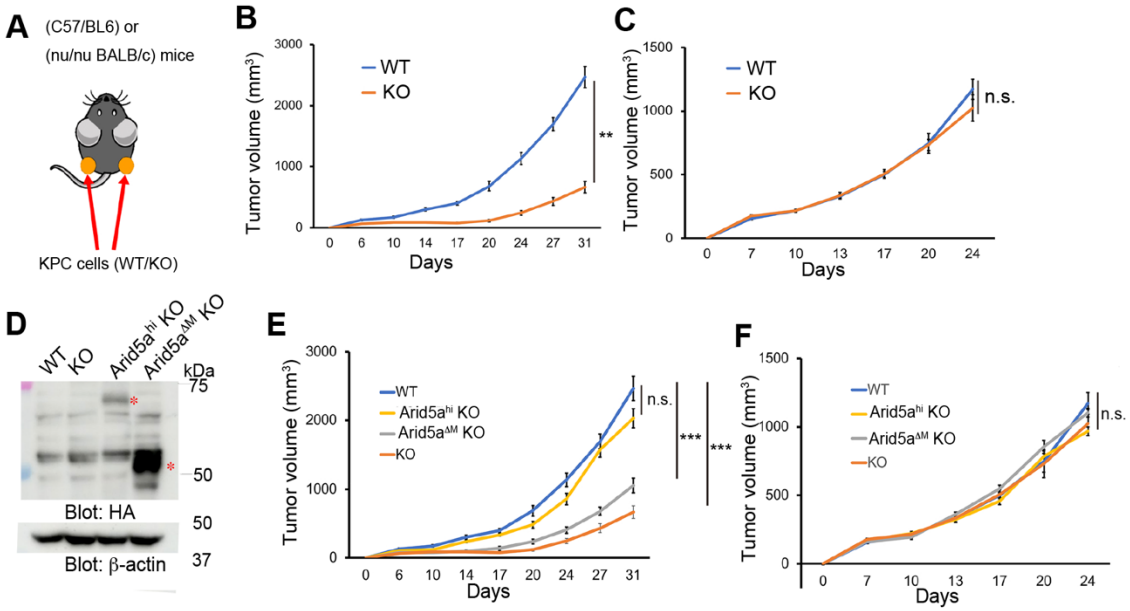

Fig. 4: Arid5a promotes immune evasion of PDAC.
A, Schematic diagram of tumor xenograft inoculation experiment. **B, C, E, F,** Analysis of cumulative tumor growth after the subcutaneous inoculation of WT or KO KPC cells into C57BL/6 (**B, E**) and nu/nu BALB/c mice (**C, F**). **D,** immunoblot analysis of the indicated proteins in WT, KO, HA-tagged Arid5a^{hi} KO and Arid5a$^{\Delta M}$ KO KPC cells. n.s., nonsignificant; $^{**}p < 0.01$, $^{***}p < 0.001$; Data are shown as the mean ± SEM, and were analyzed by two-way ANOVA. (**B, C, E, F**) Data are representative of three independent experiments with at least 6 mice per group. (**D**) Data are representative of three independent experiments.

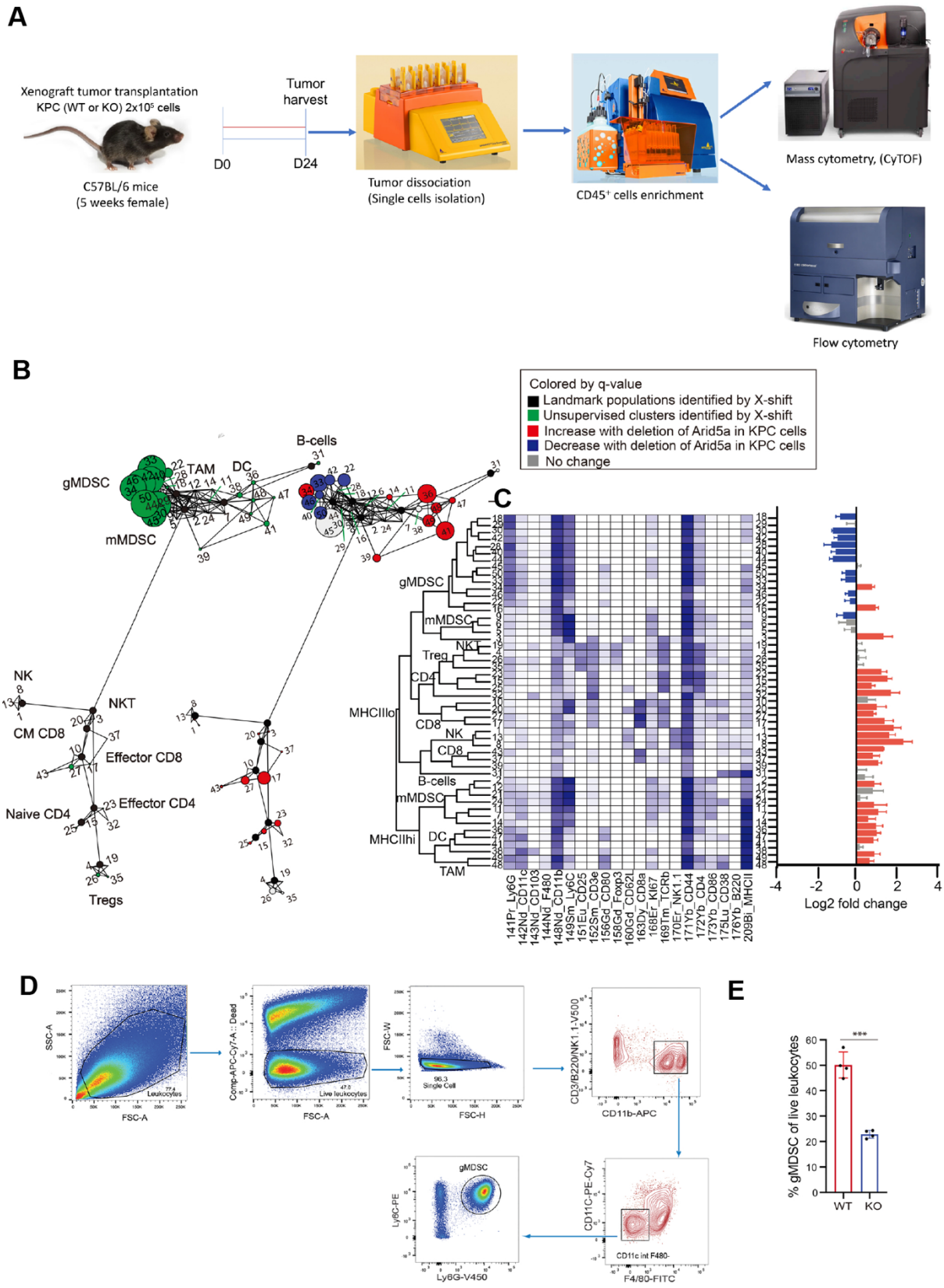

Fig. 5: Deletion of *Arid5a* suppress infiltration of immune suppressive cells and promotes anti-tumor immune cells.

A, Schematic figure showing single-cell analysis of TILs. **B** and **C,** Single-cell analysis by fixed force- and landmark-directed (SCAFFoLD) map of tumor-infiltrated CD45^{+} leukocytes.

Landmarks (black nodes) were initially identified by manual gating (**B**) or X-shift clustering (**C**), and green clusters were identified by unsupervised clustering of the data in statistical SCAFFoLD. The resulting SCAFFoLD maps were colored by statistical significance, in which features with *q*-values of less than 0.05 were considered to be statistically significant. Color by significance shows directionality of the change, i.e., red and blue indicate an increase and decrease in a particular cell subset, respectively, in the KO group. SCAFFoLD maps of TILs, $CD45^+$ leukocytes (**B**) in tumors comprising WT (left) and KO (right) KPC cells on day 21. **C,** Heatmaps (left)demonstrating the frequency of immune cells in each cluster, and graphs (right) demonstrating the significance by color. The red bars indicate significantly higher frequency of the cell population upon deletion of *Arid5a*, blue bars indicate a significantly lower frequency, and grey bars indicate no significant difference. Cluster numbers on the SCAFFoLD map correspond with the cluster numbers in the heatmap and graph. **D,** Gating strategy for the identification of gMDSCs. The lymphocytes (SSC-A versus FSC-A), singlets (FSC-W versus FSC-H), doublets (SSC-W versus SSC-H), singlets (FSC-W versus FSC-H), and live $CD3^-B220^-NK1.1^-CD11b^+CD11c^-F4/80^-$live lymphocytes were gated. The gMDSC population was determined by the surface expression of anti-Ly6C and anti-Ly6G antibodies. Data are representative of two independent experiments. **E,** Quantification of gMDSCs among live leukocytes on day 21 after the subcutaneous inoculation of KPCs, using flow cytometry.
$^{***}p < 0.001$; Data are shown as the mean ± SEM, and were analyzed by unpaired *t*-test. Data are representative of two (**B, C**), or four (**D, E**) independent experiments.

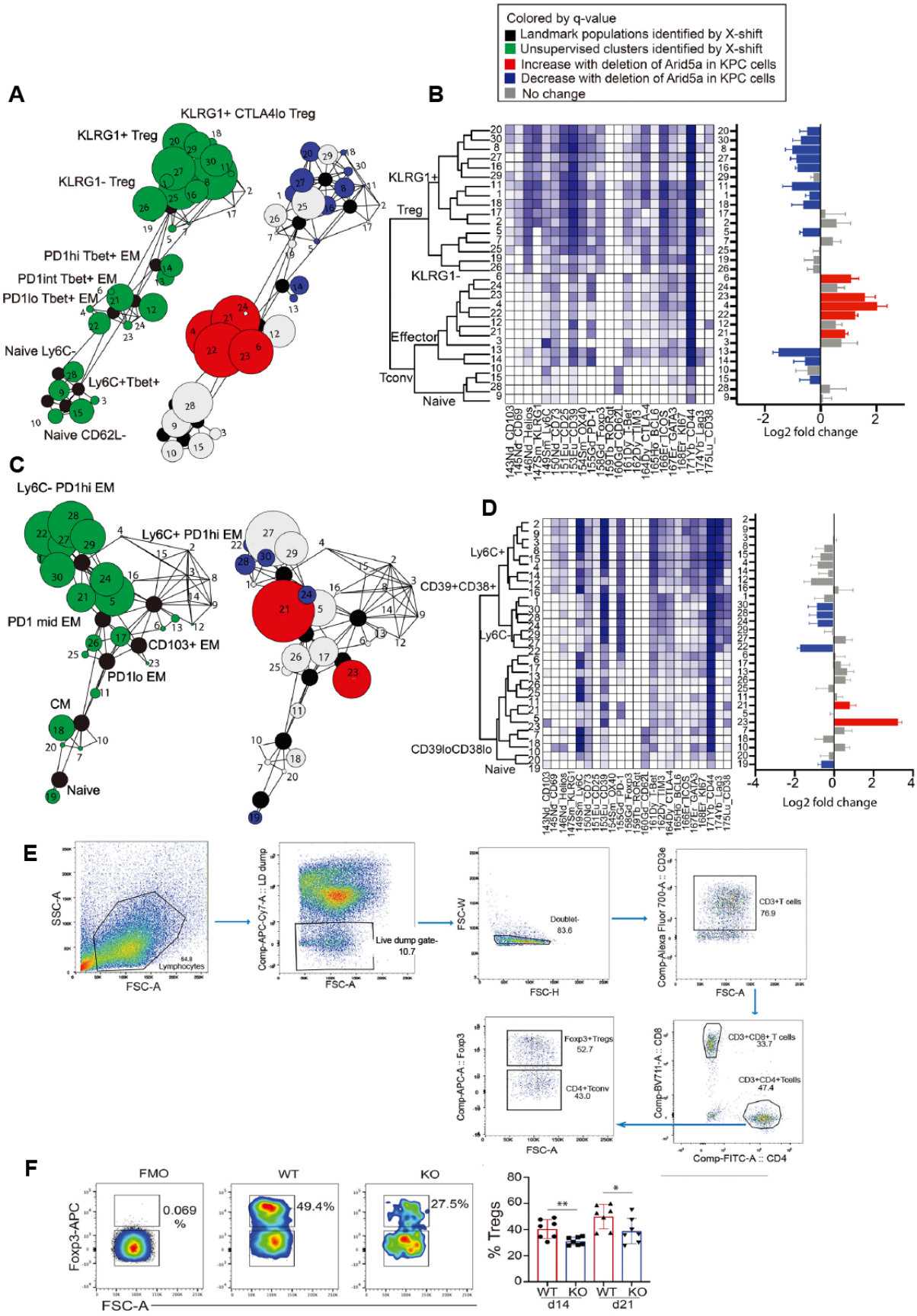

Fig. 6: Arid5a expression promotes suppressive and exhausted tumor microenvironment.

A-D, Single-cell analysis by fixed force- and landmark-directed (SCAFFoLD) map of tumor-infiltrated $CD4^+$ and $CD8^+$ T cells. Landmarks (black nodes) were initially identified by manual gating (**A**, and **C**) or X-shift clustering (**B** and **D**), and green clusters were identified by unsupervised clustering of the data in statistical SCAFFoLD. The resulting SCAFFoLD maps were colored by statistical significance, in which features with *q*-values of less than 0.05 were considered to be statistically significant. Color by significance shows directionality of the change, i.e., red and blue indicate an increase and decrease in a particular cell subset, respectively, in the KO group. SCAFFoLD maps of TILs, $CD4^+$ T-cell clusters (**A**), and $CD8^+$ T-cell clusters (**C**), in tumors comprising WT (left) and KO (right) KPC cells on day 21. **B** and **D,** Heatmaps (left)demonstrating the frequency of immune cells in each cluster, and graphs (right) demonstrating the significance by color. The red bars indicate significantly higher frequency of the cell population upon deletion of *Arid5a*, blue bars indicate a significantly lower frequency, and grey bars indicate no significant difference. Cluster numbers on the SCAFFoLD map correspond with the cluster numbers in the heatmap and graph. **E,** Gating strategy of Treg population among the TILs. T cells were identified by consecutive gating of lymphocytes (SSC-A versus FSC-A), live cells (LIVE/DEAD versus FSC-A), singlets (FSC-W versus FSC-H) and live T cells ($CD3^+$ versus FSC-A). The Treg population was determined by the intracellular expression of Foxp3 in $CD4^+$T cells. **F,** Flow cytometry analysis of the infiltrated Treg population ($Foxp3^+$ $CD4^+$ T cells) among the TILs. Foxp3 FMO staining is shown. $^*p < 0.05$, $^{**}p < 0.001$; Data are shown as the mean ± SEM, and were analyzed by unpaired *t*-test. Data are representative of two (**A-D)** or four (**E, F**) independent experiments.

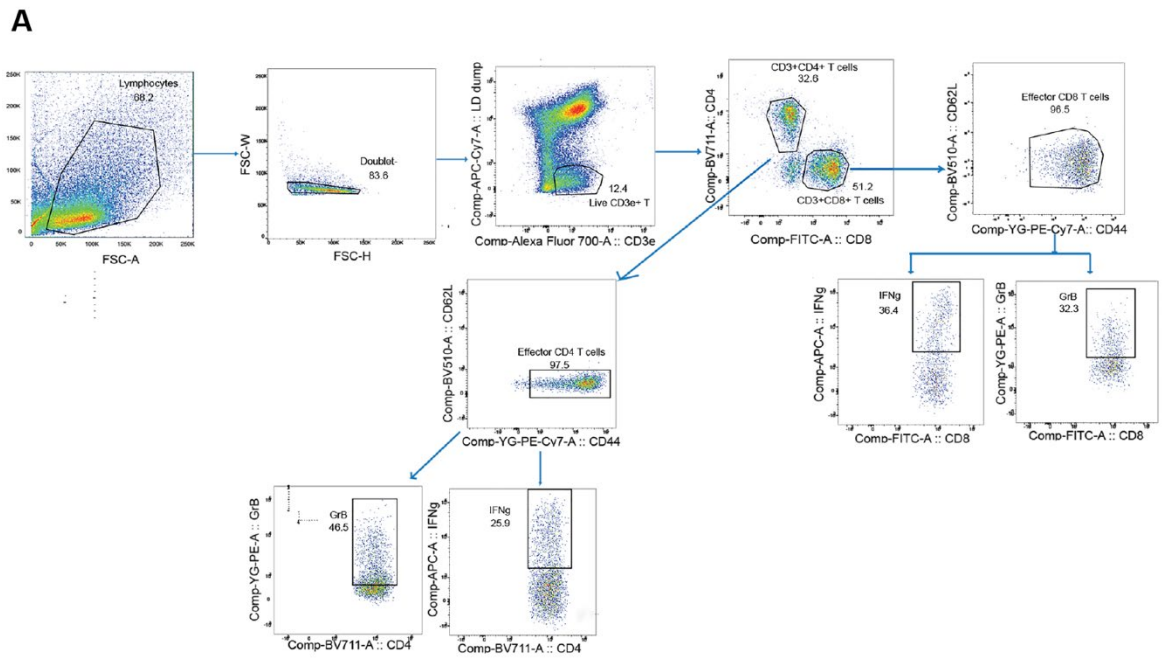

Fig. 7: Gating strategy for GzmB and IFNγ expressing CD4$^+$ T and CD8$^+$ T cells.
T cells were identified by gating of lymphocytes (SSC versus FSC), live cells (LIVE/DEAD versus FSC), singlets (FSC-W versus FSC-H), doublet- (FSC-W versus FSC-H), live CD3$^+$ T cells (LIVE/DEAD versus CD3), and effector CD8$^+$/CD4$^+$ T cells. Intracellular expression levels of IFN-γ and GzmB were determined in CD8$^+$ and CD4$^+$ T cells.

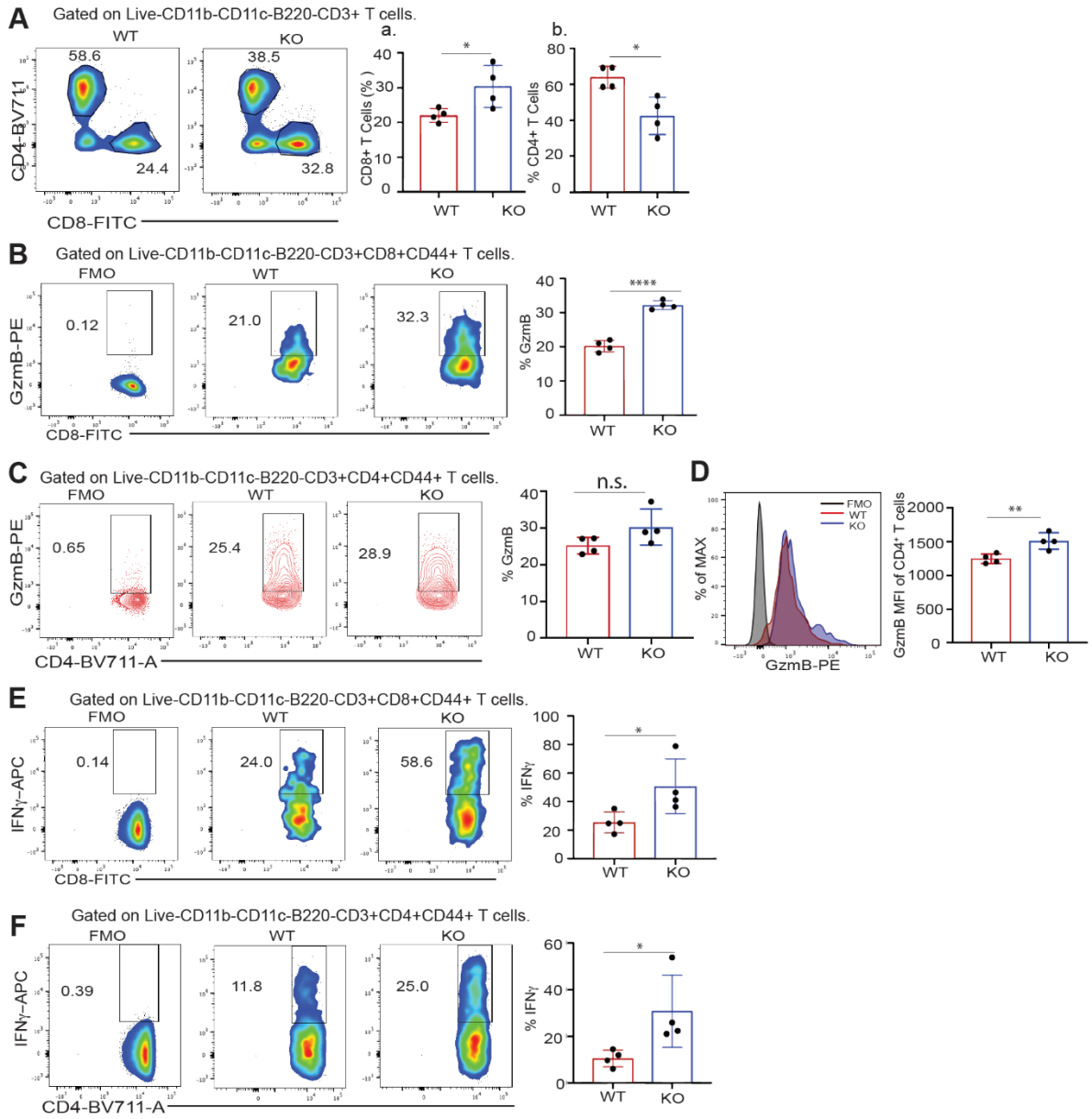

Fig. 8: Deletion of *Arid5a* induces the cytotoxic activity of tumor-infiltrating T cells. **A,** $CD8^+$ T cells (a) and $CD4^+$ T (b) cells among the TILs were analyzed by flow cytometry. **B,** Quantification by flow cytometry of GzmB expression in effector $CD8^+$ T cells among TILs. The fluorescence minus one (FMO) control is $CD44^+CD62L^-$ $CD8^+$ cells with anti-GzmB omitted. **C,** Quantification by flow cytometry of GzmB expression in effector $CD4^+$ T cells. GzmB FMO staining is shown. **D,** Mean Fluorescence Intensity (MFI) of GzmB expression in $CD4^+$ T cells were analyzed by flow cytometry. **E** and **F,** FACS analysis of IFN-γ in tumor-infiltrated effector $CD8^+$ T cells (**E**) and effector $CD4^+$ T cells (**F**). IFN-γ FMO staining is shown. n.s., nonsignificant; $^*p < 0.05$, $^{**}p < 0.01$, $^{***}p < 0.001$; Data are shown as the mean ± SEM and were analyzed by unpaired *t*-test. Data are representative of four independent experiments (**A-F**).

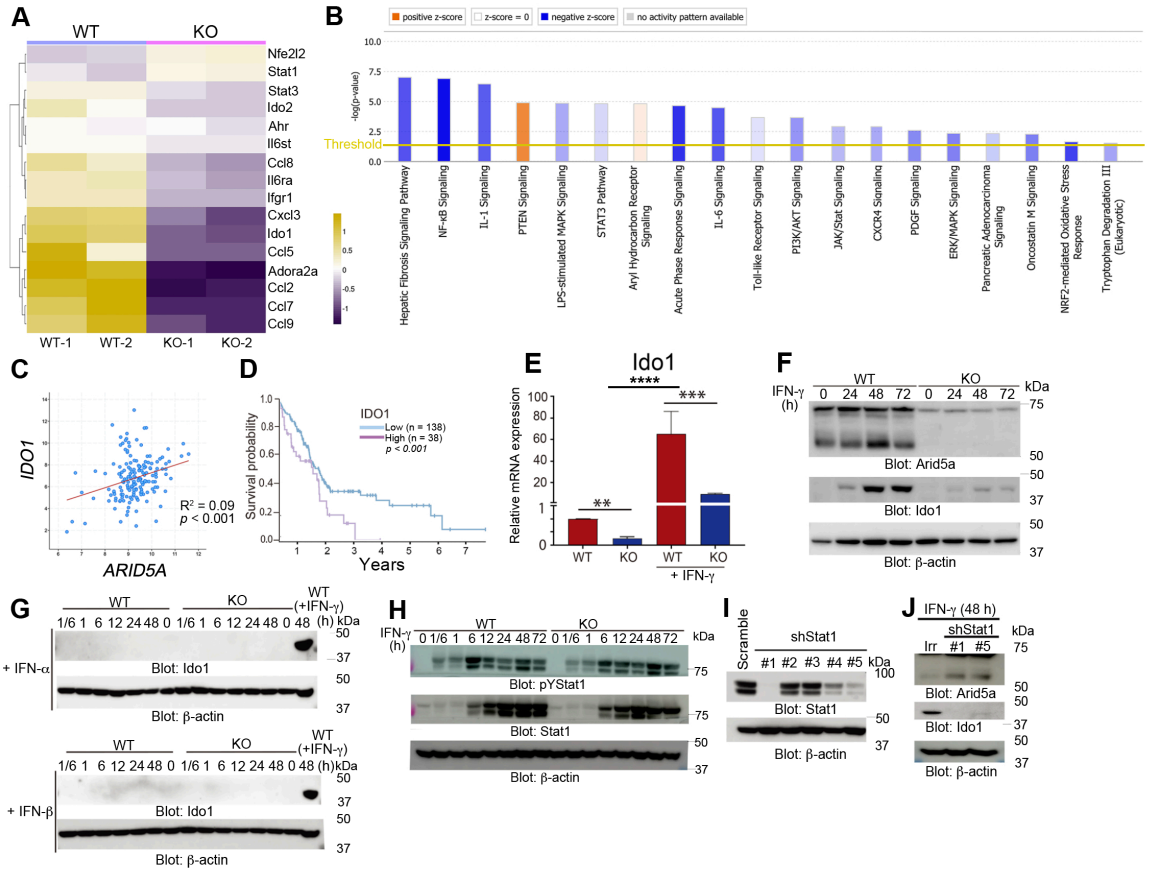

Fig. 9: Arid5a promotes IFN-γ-induced Ido1 expression.
A, Heatmap showing differentially expressed genes between WT and KO KPC cells analyzed by RNAseq. **B**, IPA of differentially expressed genes in WT cells relative to KO KPC cells. Only those genes with a fold change (FC) ≥ 2 and a false discovery rate ≤ 0.05 were used for IPA. A stronger color intensity correlates with a stronger enrichment of Z-score, both positive (orange) and negative (blue). The ratio demonstrates the proportion of genes represented in our dataset relative to all known genes in the IPA database for a given pathway. **C**, Statistical correlation of *ARID5A* and *IDO1* in the TCGA RNAseq. dataset of human primary pancreatic tumors (n = 165). The *p*-value was calculated by the Spearman rank correlation test. **D**, Kaplan-Meier curve representing the survival probability in PDAC patients from the TCGA RNAseq. dataset with regard to high or low expression levels of IDO1. The *p*-value was calculated by the log-rank test. **E,** Relative *Ido1* mRNA expression in WT and KO KPC cells untreated or treated with IFN-γ (5 ng/mL) for 48 h, measured by qRT-PCR (n = 3). **F,** WT or KO KPC cells were untreated or treated with IFN-γ, and protein expression of Arid5a and Ido1 was analyzed by immunoblotting. **G**, Immunoblot analysis of indicated proteins in WT and KO KPC cells that were treated with IFN-α or IFN-β for the indicated times. **H,** Immunoblot analysis of phosphorylated Stat1 and total Stat1 in WT and KO KPC cells, stimulated by IFN-γ for the indicated times. **I,** KPC cells were transduced with lentivirus encoding scramble or shRNA targeting *Stat1* (#1 to #5). Then, indicated protein were analyzed by immunoblot. **J,** Scramble or shStat1 KPC cells were treated with IFN-γ for 48 h and indicated proteins were analyzed using immunoblot analysis. $^{**}p < 0.01$ and $^{****}p < 0.0001$; Data are representative of three independent experiments, and are shown as the mean ± SEM as analyzed by unpaired *t*-test (**E**). Data are representative of two (**A**) or three (**F-J**) independent experiments.

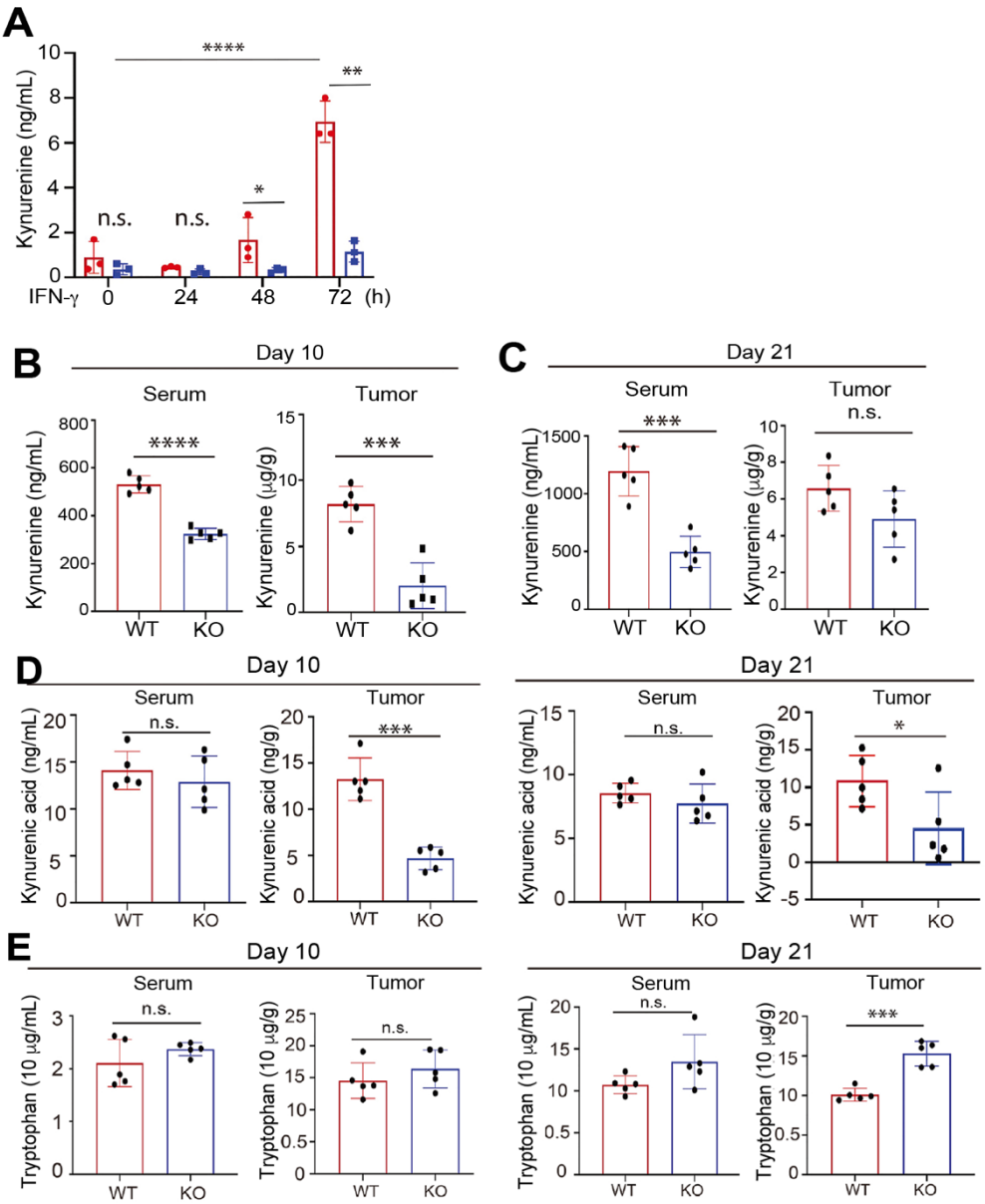

Fig. 10: Tryptophan metabolites are decreased upon deletion of *Arid5a*.
A, WT and KO KPC cells were untreated or treated with IFN-γ (5 ng/mL), and concentrations of Kyn in cell supernatants were measured by ELISA (n = 3). **B** and **C,** Levels of Kyn in tumors and sera on day 10 (**B**) and 21 (**C**) after WT and KO KPC cell inoculation was analyzed by LC-MS/MS analysis (n = 5). **D**, Levels of kynurenic acid in tumors and sera on day 10 (left) and 21 (right) after WT or KO KPC cell inoculation, determined by LC-MS/MS analysis (n = 5). **E,** Levels of Trp in tumors and sera on day 10 (left) and 21 (right) after WT and KO KPC cell inoculation, determined by LC-MS/MS metabolomics analysis (n = 5). n.s., nonsignificant; $*p < 0.05$, $**p < 0.01$, and $***p < 0.001$; (**A–E**) Data are cumulative of five independent experiments done in duplicates (n=10). Data are shown as the mean ± SEM, and were analyzed by one way ANOVA with post-hoc Tukey's test (**A**) or unpaired *t*-test (**B-E**).

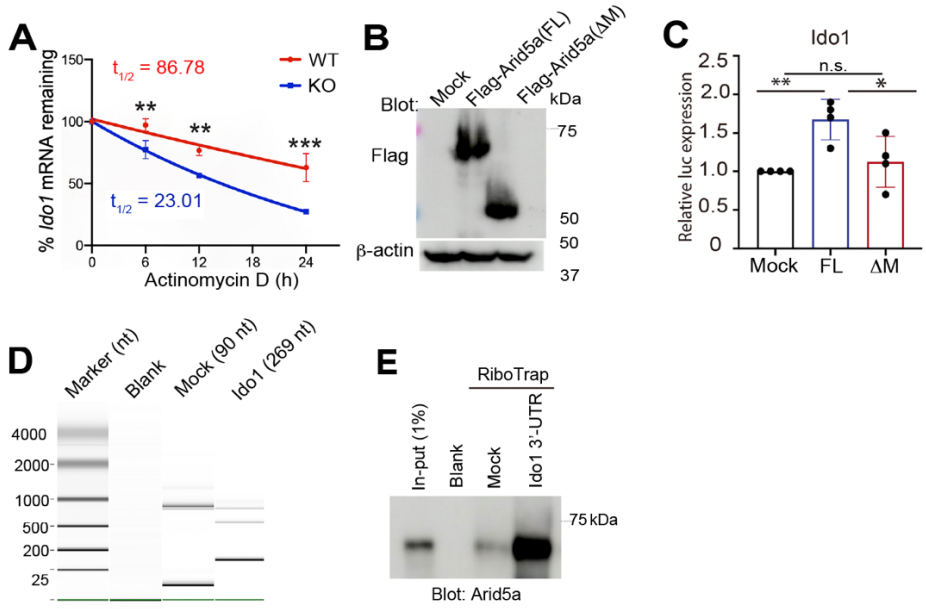

Fig. 11: Arid5a stabilizes *Ido1* mRNA by binding to its 3'-UTR

A, Relative *Ido1* mRNA levels remaining in WT and KO KPC cells cultured under IFN-γ stimulation for 6 h, followed by actinomycin D treatment for 0 to 24 h, were compared with each mRNA expression level at 0 h. **B**, KO KPC cells were transfected with empty vector, Flag-Arid5a (FL), or Flag-Arid5a (ΔM). After 24 h, lysates were collected and subjected to immunoblotting analysis of the indicated proteins. **C,** Measurement of the luciferase activity of KO KPC cells 48 hours after transfection with luciferase reporter plasmid expressing the *Ido1* 3′-UTR together with control plasmid (Mock) or an expression plasmid for full-length (FL) or deletion mutant (ΔM) of Arid5a. Results are presented relative to Renilla luciferase activity. **D**, Quality checking of *in vitro* synthesized RNAs, encoding the 3′-UTR of *Ido1* and vector alone. **E,** immunoblot analysis of Arid5a binding to Ido1 3'UTR using RipoTrap assay. n.s., nonsignificant; $^{*}p < 0.05$, $^{**}p < 0.01$ and $^{***}p < 0.001$; Data are shown as the mean ± SEM, and were analyzed were analyzed by one-way ANOVA with post-hoc Tukey's test (**A, C**). Data are representative of three independent experiments (**A**–**E**).

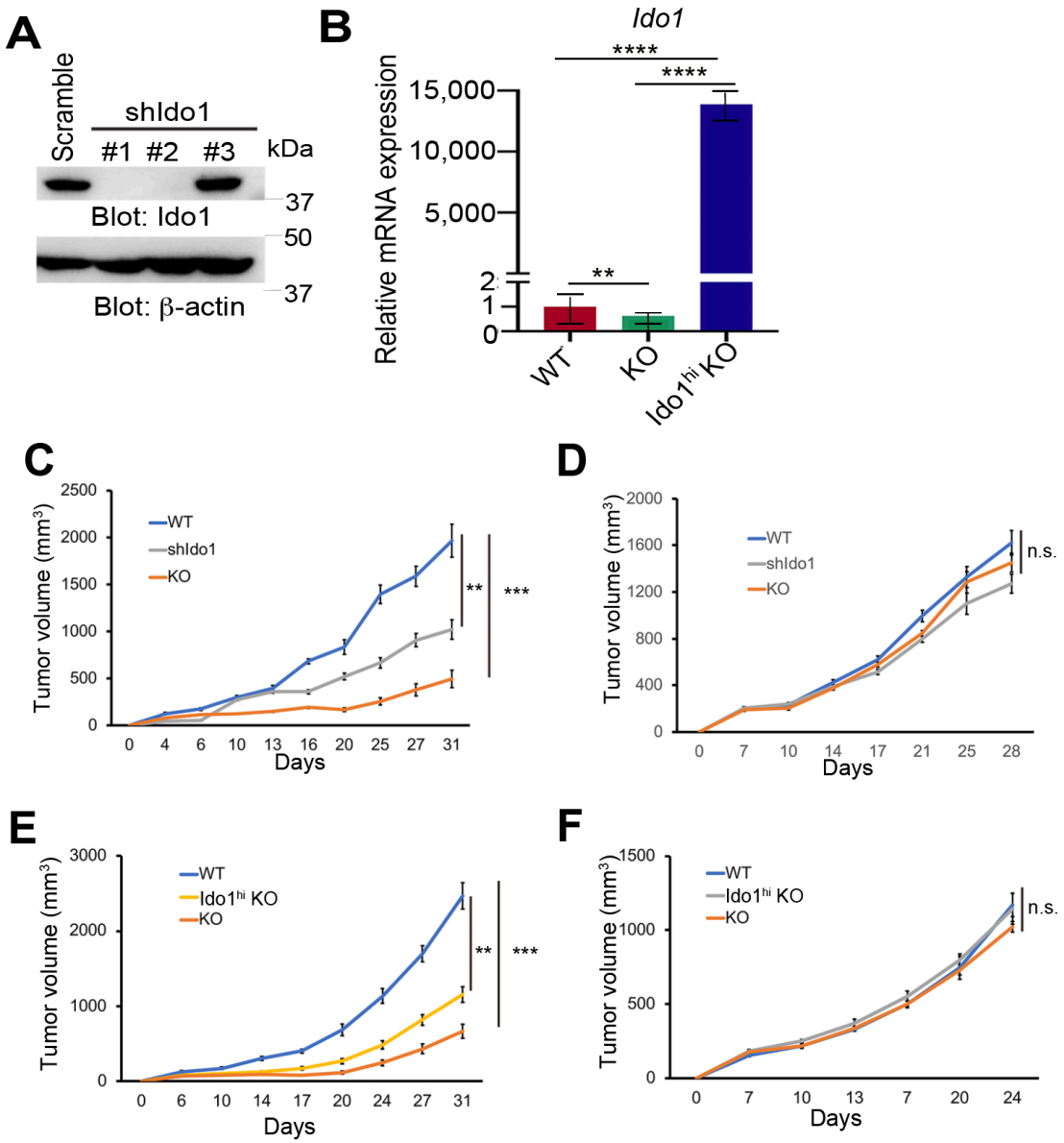

Fig. 12: Arid5a regulates tumor growth partially through Ido1-kyn axis.
A, KPC cells were transduced with lentivirus encoding scramble or shRNA targeting *Ido1,* followed by IFNγ stimulation (5 ng/ml). Then, indicated protein were analyzed by immunoblot. **B**, Relative expression levels of *Ido1* mRNA in WT, KO, and Ido1^{hi} KO KPC cells as measured by qRT-PCR. **C-F,** Analysis of cumulative tumor growth after the subcutaneous xenograft inoculation of indicated KPC ($2x10^5$) cells into C57BL/6 (**C** and **E**) and nu/nu BALB/c mice (**D** and **F**). n.s., nonsignificant; $^{**}p < 0.01$, $^{***}p < 0.001$ and $^{****}p < 0.0001$; **(A and B)** Data are representative of three independent experiments. **(C-F)** Data are representative of three independent experiments with at least 6 mice per group. Data are shown as the mean ± SEM, and were analyzed by one-way ANOVA with post-hoc Tukey's test (**B**) or two-way ANOVA (**C-F**).

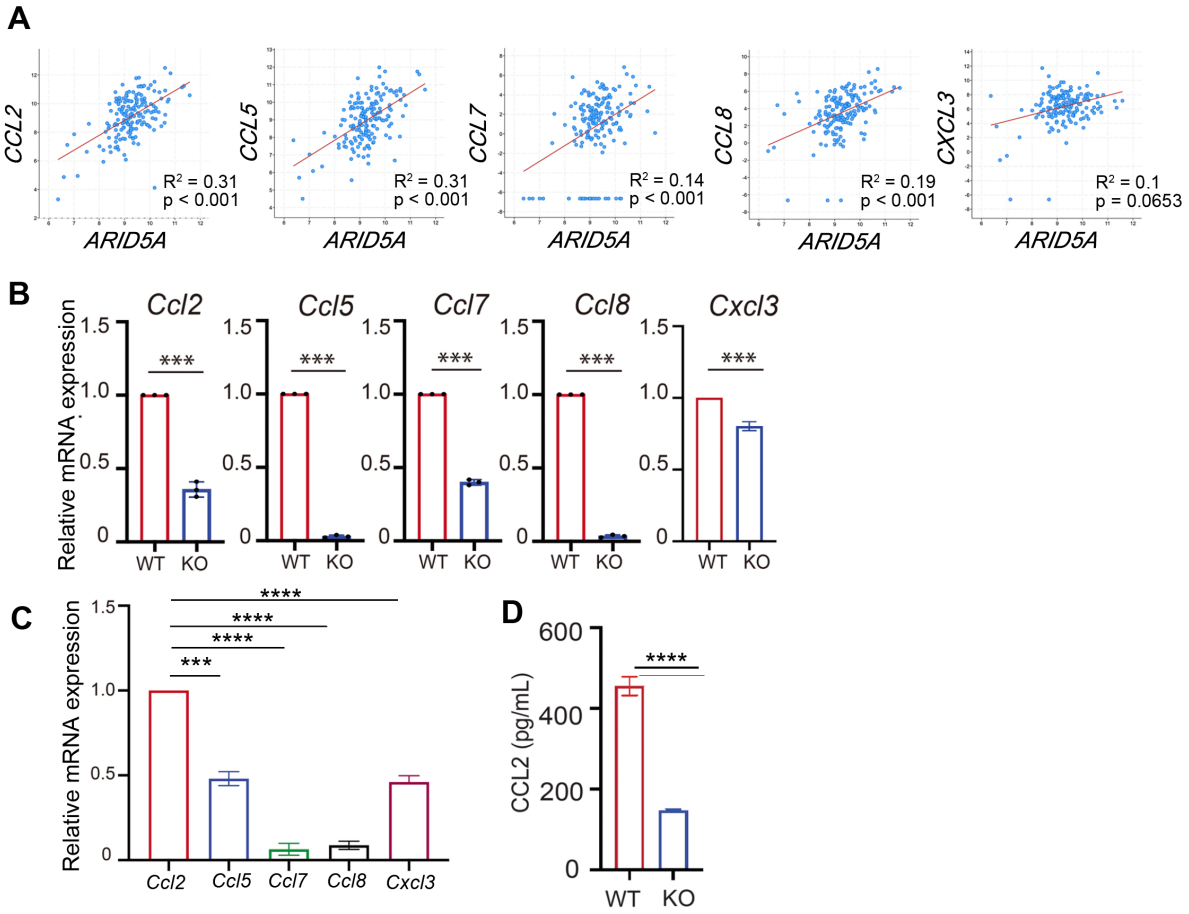

Fig. 13: Arid5a stabilizes *Ccl2* mRNA and promotes Ccl2 expression in KPC cells.
A, Statistical correlation of the expression levels of ARID5A and chemokines, such as *CCL2, CCL5, CCL7, CCL8*, and *CXCL3*, in the TCGA RNAseq. dataset of human primary pancreatic tumors (n = 165). The *p*-values were analyzed by the Spearman rank correlation test. **B,** Relative mRNA expression levels of chemokines in WT and KO KPC cells as measured by qRT-PCR. **C**, Relative mRNA expression of the indicated chemokines in WT KPC cells as measured by qRT-PCR.. **D,** Ccl2 protein levels in WT and KO KPC cell supernatants were measured by ELISA. $^{***}p < 0.001$ and $^{****}p < 0.0001$; Data are shown as the mean ± SEM, and were analyzed by the unpaired *t*-test (**B, D**) and one-way ANOVA with post-hoc Tukey's test (**C**). (**B-D**) Data are representative of three independent experiments.

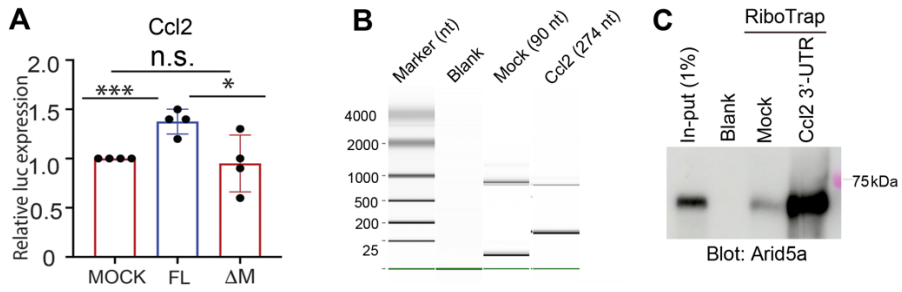

Fig. 14: Arid5a stabilizes *Ccl2* mRNA binding to its 3'-UTR.
A, KO KPC cells were transfected with luciferase reporter plasmid expressing the *Ccl2* 3′-UTR together with control plasmid (Mock) or an expression plasmid for full-length (FL) or deletion mutant (ΔM) of Arid5a. Cells were lysed after 48 h and the luciferase activity was measured. Results are presented relative to Renilla luciferase activity. **B**, Quality checking of *in vitro* synthesized RNAs, encoding the 3′-UTR of *Ccl2* and vector alone, using a 2100 Bioanalyzer (Agilent Technologies). **C,** Immunoblot analysis of Arid5a binding to Ccl2 3'UTR using RipoTrap assay. n.s., nonsignificant; $^{*}p < 0.05$ and $^{***}p < 0.001$; Data are shown as the mean ± SEM, and were analyzed by one-way ANOVA with post-hoc Tukey's test (**A**). (**A-C**) Data are representative of three independent experiments.

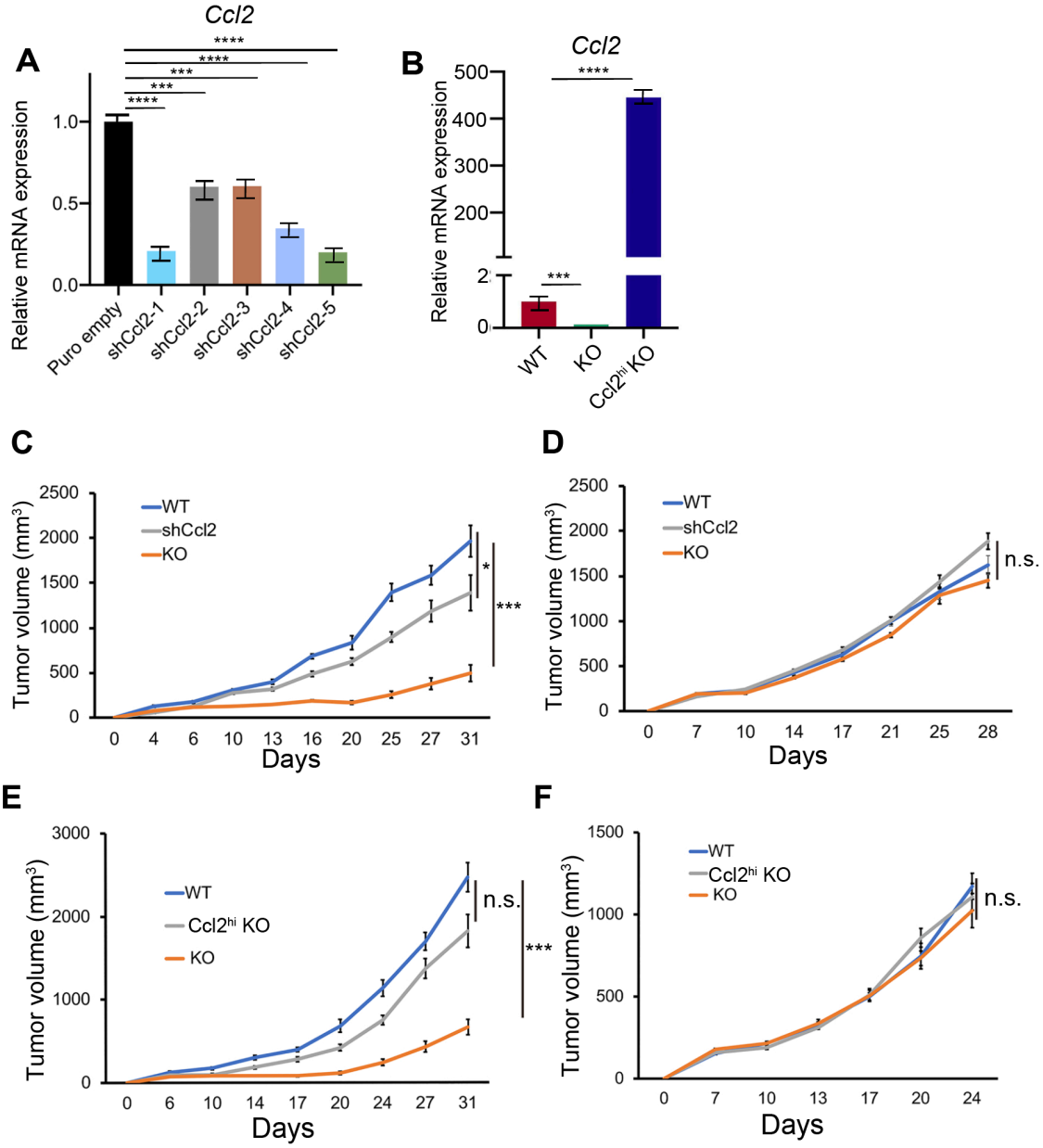

Fig. 15: Arid5a regulates tumor growth through regulating Ccl2.
A, KPC cells were transduced with lentivirus encoding scramble or shRNA targeting *Ccl2.* Then, relative expression levels of *Ccl2* mRNA was measured by qRT-PCR. **B,** Relative mRNA levels of *Ccl2* expressed in WT, KO, and Ccl2^{hi} KO KPC cells as measured by qRT-PCR. **C-F,** Analysis of cumulative tumor growth after the subcutaneous xenograft inoculation of indicated KPC cells (2x10^5) into C57BL/6 (**C** and **E**) and nu/nu BALB/c mice (**D** and **F**). n.s., nonsignificant; $^*p < 0.05$, $^{***}p < 0.001$, and $^{****}p < 0.0001$; **(A and B)** Data are representative of three independent experiments. **(C-F)** Data are representative of three independent experiments with at least 6 mice per group. Data are shown as the mean ± SEM, and were analyzed by by one-way ANOVA with post-hoc Tukey's test (**A and B**) or two-way ANOVA (**C-F**).

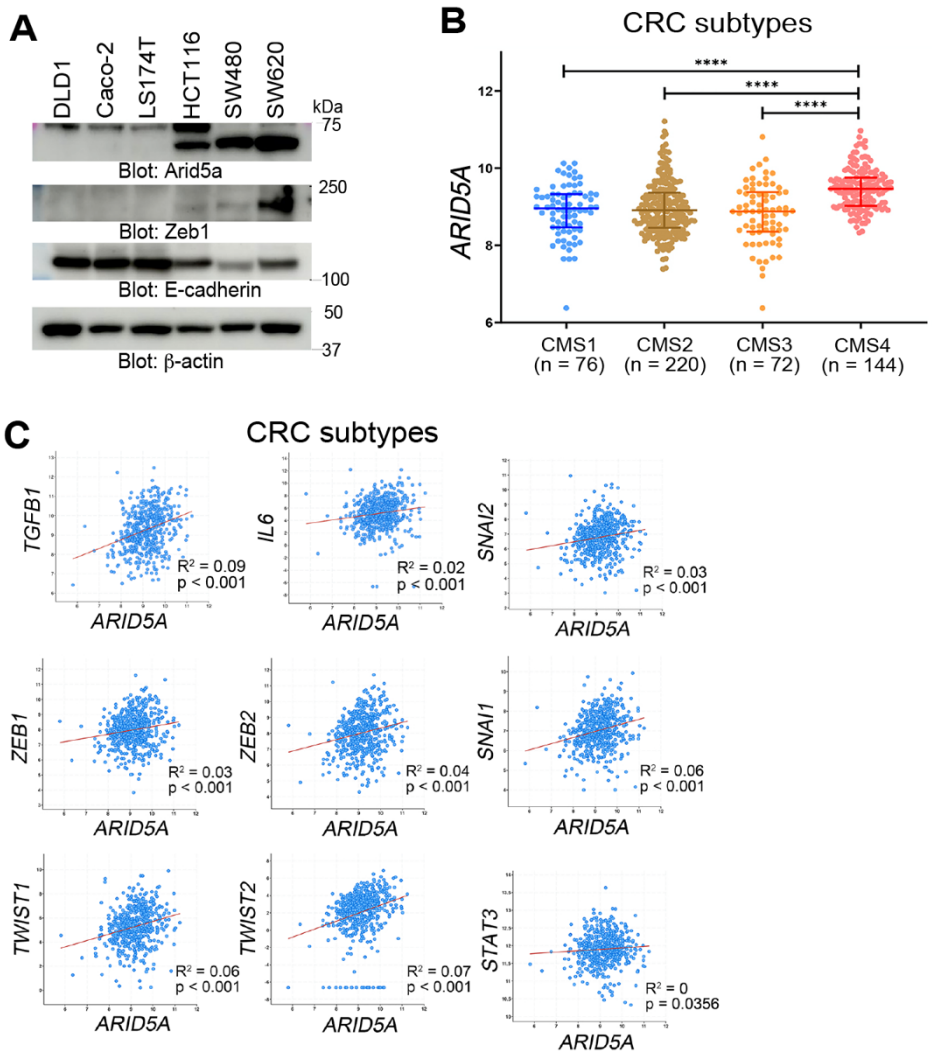

Fig. 16: Arid5a is expressed in mesenchymal tumor subtypes of colorectal tumors.
A, Immunoblot analysis of the indicated proteins in representative human CRC cell lines. **B**, ARID5A mRNA expression levels among the various CRC subtypes as measured by RNAseq. **C**, Statistical correlation of the expression levels of ARID5A and indicated EMT associated genes in the TCGA RNAseq. dataset of human colorectal tumors (n = 597). ****$p <$ 0.0001; Data are shown as the mean ± SEM, and were analyzed by one way ANOVA (**B**). Data are representative of three independent experiments (**A**).

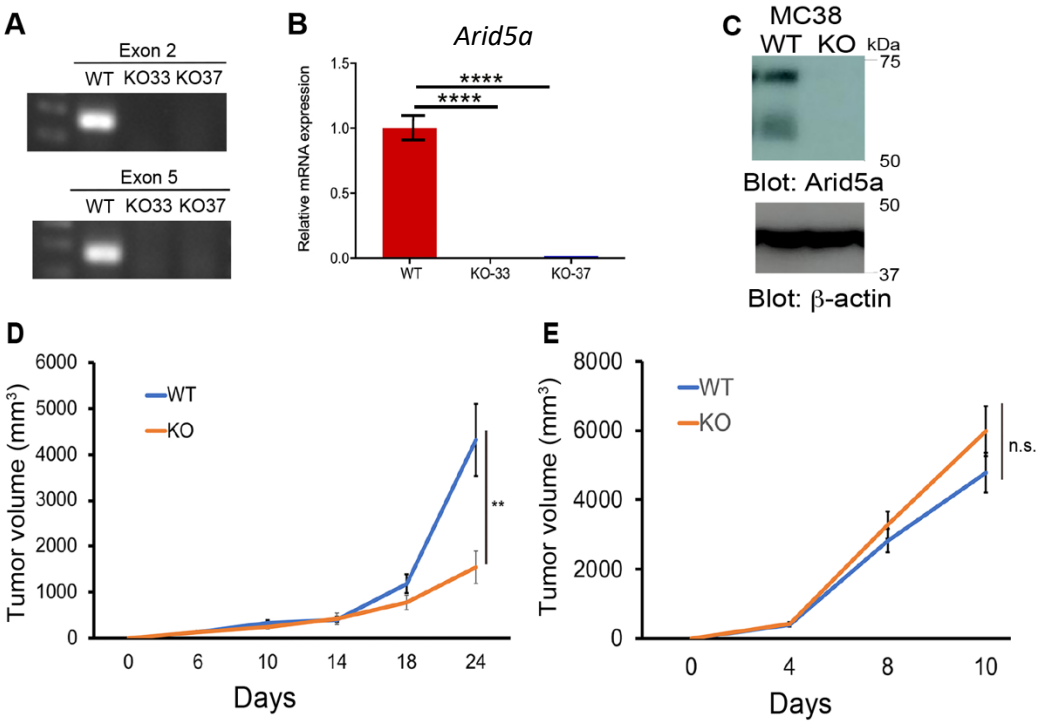

Fig. 17: Arid5a promotes immune evasion of colorectal cancer.
A, Expression of *Arid5a* indicated exons in MC38 as analyzed by genomic PCR. **B,** *Arid5a* mRNA expression in WT and KO MC38 cells as analyzed by qRT-PCR. **C,** Immunoblot analysis of indicated proteins in WT and KO MC38 cells. **D** and **E,** Analysis of cumulative tumor growth after the subcutaneous xenograft inoculation of WT or KO MC38 cells ($1x10^5$) into C57BL/6 (**D**) and nu/nu BALB/c mice (**E**). $^{**}p < 0.005$, $^{****}p < 0.0001$; Data are shown as the mean ± SEM, and were analyzed by one way ANOVA with post-hoc Tukey's test. (**A-C**) Data are representative of three independent experiments**. (D and E)** Data are representative of three independent experiments with at least 6 mice per group.

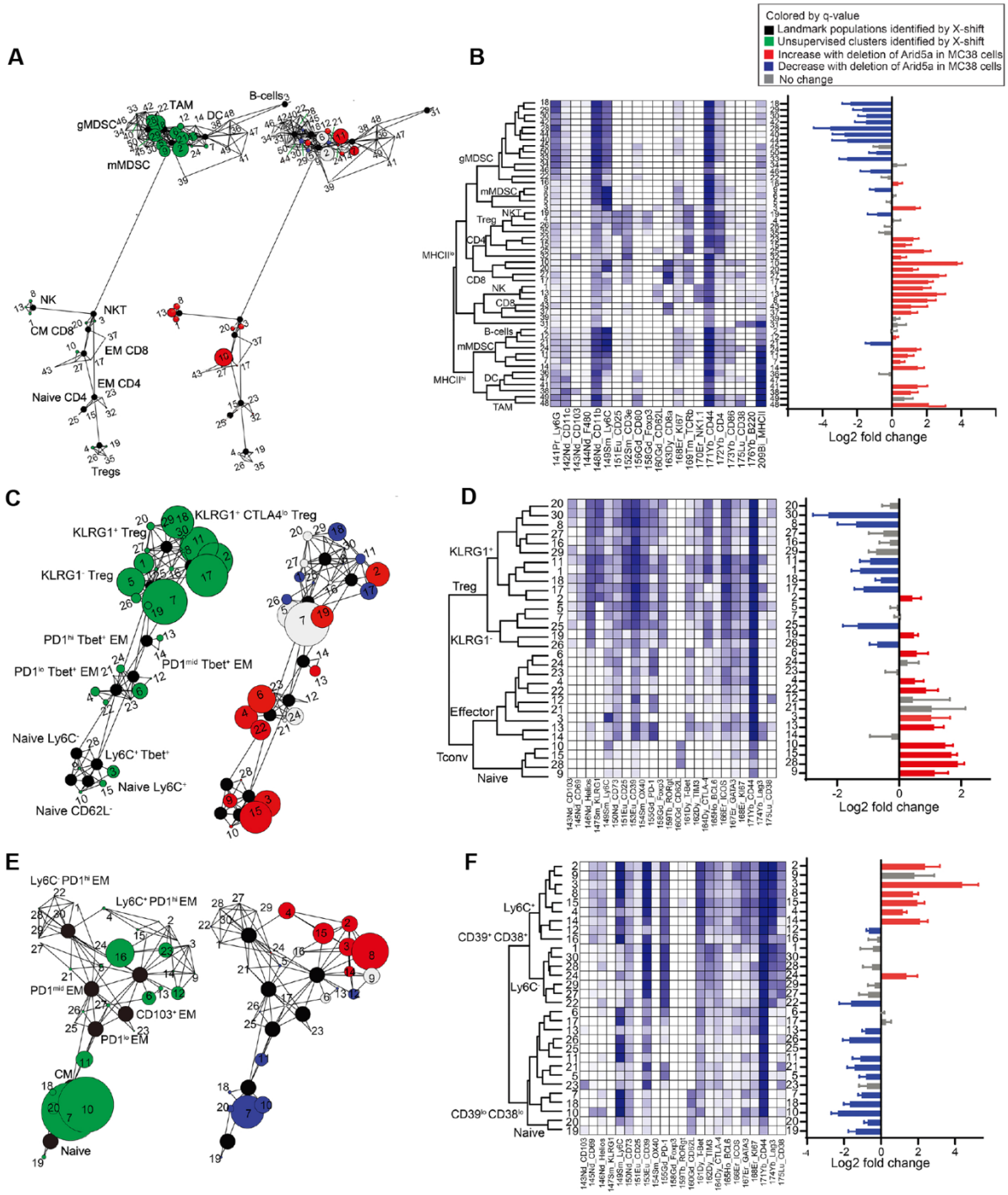

Fig. 18: Arid5a enhances suppressive tumor microenvironment in MC38 tumor.
A, C, and **E,** SCAFFoLD map of tumor-infiltrated CD45$^+$ leukocytes (**A**), CD4$^+$ T-cell clusters (**C**), and CD8$^+$ T-cell clusters (**E**), in tumors derived from WT (left) and KO (right) MC38 cells on day 14. **B, D,** and **F,** Heatmaps (left) showing the frequency of immune cells in each cluster and graphs (right) showing significance by color compared with cells from KO MC38 tumors. Cluster numbers on the SCAFFoLD map correspond with cluster numbers in the heatmaps and graphs. (**A-F**) Data are representative of two independent experiments.

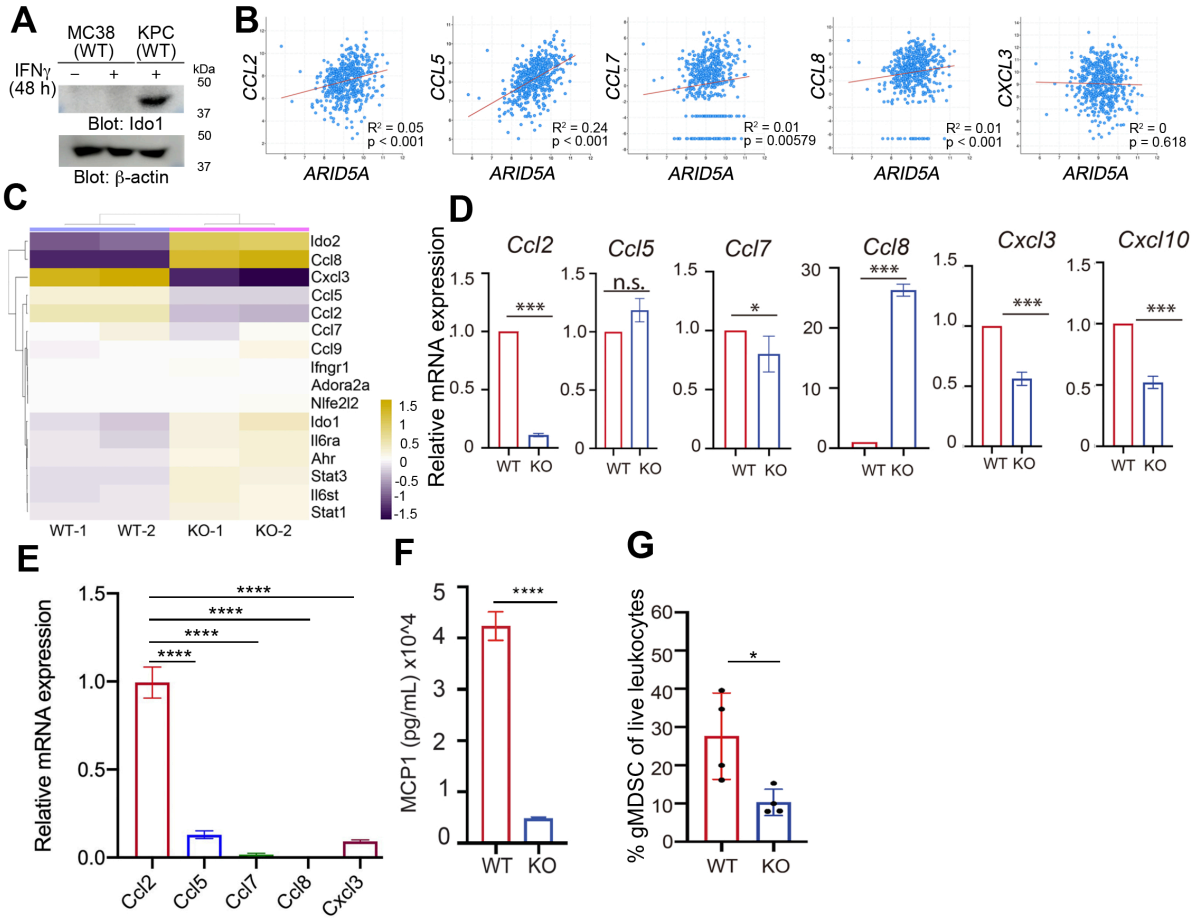

Fig. 19: Arid5a promotes chemokine expression in MC38 cells.
A, Immunoblot analysis of indicated proteins in WT and KO MC38 cells, and WT KPC cells untreated or treated with IFN-γ for 48 h. **B,** Statistical correlation of the expression levels of ARID5A and chemokines, in the TCGA RNAseq. dataset of human primary CRCs (n = 597). *p*-values were calculated by the Spearman rank correlation test. **C,** Heatmap showing differentially expressed genes between WT and KO MC38 cells, measured by RNAseq. **D,** Relative mRNA expression levels of the indicated chemokines in WT and KO MC38 cells as measured by qRT-PCR. **E,** Relative mRNA expression levels of the indicated chemokines in WT MC38 cells as measured by qRT-PCR. **F,** MCP1 (Ccl2) protein levels in WT and KO MC38 cell supernatants were measured by ELISA. **G,** Quantification of gMDSCs among live TILs on day 14 after the subcutaneous xenograft inoculation of MC38 cells as measured by flow cytometry. n.s., nonsignificant; $^{*}p < 0.05$, $^{***}p < 0.001$, and $^{****}p < 0.0001$; Data are shown as the mean ± SEM, and were analyzed by the unpaired *t*-test (**D, F** and **G**) and one-way ANOVA with post-hoc Tukey's test (**E**). Data are representative of three (**A, D-G**) or two (**C**) independent experiments.

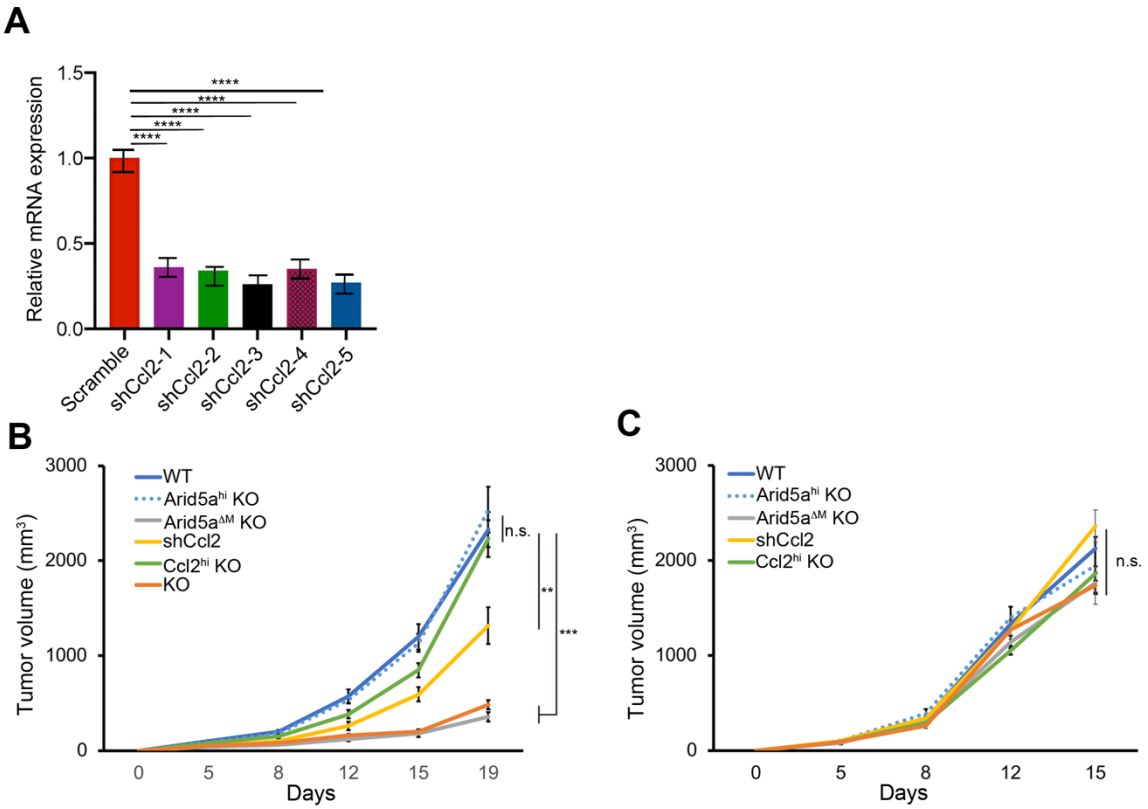

Fig. 20: Arid5a promotes tumor growth in MC38 cells through regulation of Ccl2. **A,** MC38 cells were transduced with lentivirus encoding scramble or shRNA targeting *Ccl2*. Then, relative expression levels of *Ccl2* mRNA was measured by qRT-PCR. **B** and **C,** Analysis of cumulative tumor growth after the subcutaneous xenograft inoculation of MC38 ($1x10^5$) cells into C57BL/6 (**B**) and nu/nu BALB/c mice (**C**). n.s., nonsignificant; $^{*}p < 0.05$, $^{***}p < 0.001$, and $^{****}p < 0.0001$; Data are shown as the mean ± SEM, and were analyzed by by one-way ANOVA with post-hoc Tukey's test (**A**) or two-way ANOVA (**B and C**). (**A**) Data are cumulative of three independent experiments. (**B and C**) Data are representative of three independent experiments with at least 6 mice per group.

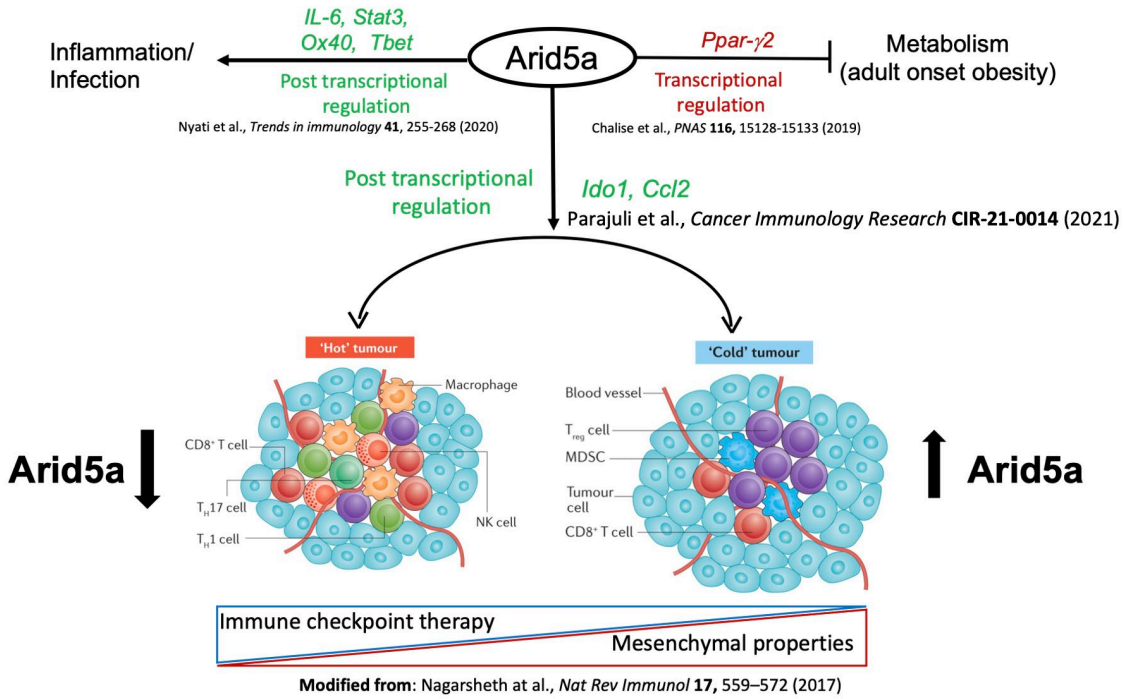

Fig. 21: Schematic diagram showing Arid5a functions.
Arid5a regulates different molecules at both transcriptional or post-transcriptional level. As a transcriptional function, it binds to promoter of *Ppar-γ2* and represses its metabolic activity. As a post-transcriptional activity, Arid5a binds to the 3'-UTR and stabilizes mRNAs of different molecules that induce inflammation and infection such as *IL-6, Stat3, Tbet*. In mesenchymal tumors, Arid5a post-transcriptionally stabilizes Ido1 and Ccl2 mRNAs, which promotes immune evasion.

Academic accomplishments:

Journal Publications

1. **Parajuli, G**., Tekguc, M., Wing, J.B., Hashimoto, A., Okuzaki, D., Hirata, T., Sasaki, A., Itokazu, T., Handa, H., Sugino, H., Nishikawa, Y., Metwally H., Kodama, Y., Tanaka, S., Sabe, H., Yamashita, T., Sakaguchi, S., Kishimoto, T., and Hashimoto, S. (2021) Arid5a promotes immune evasion by augmenting tryptophan metabolism and chemokines expression. Cancer Immunology Research, CIR-21-001. **DOI:** 10.1158/2326-6066.CIR-21-0014

2. Metwally, H., Tanaka, T., Li, S., **Parajuli, G**., Kang, S., Hanieh, H., Hashimoto, S., Chalise, J.P., Gemechu, Y., Standley, D.M. and Kishimoto, T. (2020). Noncanonical STAT1 phosphorylation expands its transcriptional activity into promoting LPS-induced IL-6 and IL-12p40 production. Science signaling, 13(624). **DOI**: 10.1126/scisignal.aay0574

3. Hashimoto, S., Furukawa, S., Hashimoto, A., Tsutaho, A., Fukao, A., Sakamura, Y., **Parajuli, G.,** Onodera, Y., Otsuka, Y., Handa, H., Oikawa, T., Hata, S., Nishikawa, Y., Mizukami, Y., Kodama, Y., Murakami, M., Fujiwara, T., Hirano, S., and Sabe, H. (2019). ARF6 and AMAP1 are major targets of KRAS and TP53 mutations to promote invasion, PD-L1 dynamics, and immune evasion of pancreatic cancer. Proceedings of the National Academy of Sciences, 116(35), 17450-17459. **DOI**: 10.1073/pnas.1901765116

4. Chalise, J.P., Hashimoto, S., **Parajuli, G.,** Kang, S., Singh, S.K., Gemechu, Y., Metwally, H., Nyati, K.K., Dubey, P.K., Zaman, M.M.U. and Nagahama, Y., Hamza, H., Masuda, K., and Kishimoto, T. (2019). Feedback regulation of Arid5a and Ppar-γ2 maintains adipose tissue homeostasis. Proceedings of the National Academy of Sciences, 116(30), 15128-15133. **DOI**: 10.1073/pnas.1906712116

5. Gemechu, Y., Millrine, D., Hashimoto, S., Prakash, J., Sanchenkova, K., Metwally, H., **Parajuli, G**., Kang, S. and Kishimoto, T. (2018). Humanized cereblon mice revealed two distinct therapeutic pathways of immunomodulatory drugs. Proceedings of the National Academy of Sciences, 115(46), 11802-11807. **DOI**: 10.1073/pnas.1814446115

Conference Presentations

1. **Parajuli, G**., Hashimoto, S., & Kishimoto, T. Arid5a orchestrates immune evasion of pancreatic cancer via the Ido1-–mediated tryptophan metabolism. *J Immunol* May 1, 2020, 204 (1 Supplement) 240.5; Hawaii, USA. (Nominated for Poster and Oral presentation)

2. **Parajuli, G**., Hashimoto, S., and Kishimoto, T. Arid5a orchestrates immunosuppressive environment via the Ido1-kynurenine-Treg axis in malignant pancreatic cancer. December, 2019 (48th Annual Meeting of Japanese Society for Immunology); Hamamatsu, Japan. (Poster and Oral presentations)

3. **Parajuli, G.** Arid5a orchestrates immunosuppressive environment via Ido-kynurenine-Treg axis in malignant pancreatic cancer. The 586th Biken Monthly Seminar on June 25, 2019, Osaka University, Osaka, Japan. (Oral presentation)

4. Poudel, K., **Parajuli, G.** and Poudel, B. (2015) The impact of government supported hemodialysis on patient outcomes in the Western Region of Nepal. March, 2015 (World Congress of Nephrology, Cape town, South Africa). (Poster presentation)

Acknowledgement

I would like to express my gratitude to my advisor Prof. Tadamitsu Kishimoto, for believing in me and continuously supporting me throughout this entire journey. I would like to thank him for the valuable comments, remarks, and engagement through the learning process of this Ph.D. thesis. His insights on both my research and career are invaluable. I could not have imagined having a better advisor for study.

I would also like to thank Dr. Shigeru Hashimoto for being my mentor with all his patience and motivation. Dr. Hashimoto has been always welcoming whenever I ran into trouble during experiments or had a question about my research or writing. He consistently allowed this paper to be my work but always suggested the right direction whenever he thought I needed it. Without his passionate participation and input, this project could not have been successfully conducted.

Additionally, I would like to thank the experts in my lab and in the IFReC who were involved in this research. Their positive response and suggestions were always motivating. I must express my profound gratitude to my parents, brother, and sweetest boyfriend for providing me with unfailing support and continuous encouragement throughout my years of study.